Defense Threat Reduction Agency
8725 John J. Kingman Road, MS
6201 Fort Belvoir, VA 22060-6201

TECHNICAL REPORT

Impact Response of Granular Material at Global and Meso Scales

Approved for public release, distribution is unlimited.

February 2013

Wayne Chen and Dimitri
Peroulis

Prepared by:
Purdue University
701 West Stadium Avenue
West Lafayette, IN 47907

REPORT DOCUMENTATION PAGE

Form Approved
OMB No. 0704-0188

Public reporting burden for this collection of information is estimated to average 1 hour per response, including the time for reviewing instructions, searching existing data sources, gathering and maintaining the data needed, and completing and reviewing this collection of information. Send comments regarding this burden estimate or any other aspect of this collection of information, including suggestions for reducing this burden to Department of Defense, Washington Headquarters Services, Directorate for Information Operations and Reports (0704-0188), 1215 Jefferson Davis Highway, Suite 1204, Arlington, VA 22202-4302. Respondents should be aware that notwithstanding any other provision of law, no person shall be subject to any penalty for failing to comply with a collection of information if it does not display a currently valid OMB control number. PLEASE DO NOT RETURN YOUR FORM TO THE ABOVE ADDRESS.

1. REPORT DATE (DD-MM-YYYY) 18-07-2012	2. REPORT TYPE Technical	3. DATES COVERED (From - To) 25-03-2009 to 07-04-2012

4. TITLE AND SUBTITLE	5a. CONTRACT NUMBER
Impact Response of Granular Material at Global and Meso Scales	
	5b. GRANT NUMBER HDTRA1-09-1-0037
	5c. PROGRAM ELEMENT NUMBER

6. AUTHOR(S)	5d. PROJECT NUMBER
Wayne Chen, Dimitri Peroulis	
	5e. TASK NUMBER
	5f. WORK UNIT NUMBER

7. PERFORMING ORGANIZATION NAME(S) AND ADDRESS(ES)	8. PERFORMING ORGANIZATION REPORT NUMBER
Purdue University, 701 West Stadium Avenue, West Lafayette, IN 47907-2045	

9. SPONSORING / MONITORING AGENCY NAME(S) AND ADDRESS(ES)	10. SPONSOR/MONITOR'S ACRONYM(S)
Defense Threat Reduction Agency, 8725 John J. Kingman Road, MSC 6201, Ft Belvoir, VA 220060-6201	DTRA
	11. SPONSOR/MONITOR'S REPORT NUMBER(S) DTRA-TR-12-66

12. DISTRIBUTION / AVAILABILITY STATEMENT

Approved for public release; distribution is unlimited.

13. SUPPLEMENTARY NOTES

14. ABSTRACT

The objective of this research program is to develop fundamental understanding of the mechanical response of granular target materials under impact loading conditions at two scales: continuum level and particulate level. Complicated interactions between the granular target and a high-speed projectile may produce unexpected projectile motion. A physical and quantitative understanding of the granular material behavior will significantly contribute to the optimal manipulation of the projectile-target interactions in high-speed penetration. In this program, we conducted sand penetration experiments at global scale with the positions of the projectile monitored by flash x-ray. To observe variations in impact-induced pressure inside the sand target, we developed thin pressure sensors that are embedded in strategic locations and wireless communication system to wirelessly connect the sensors to data-acquisition systems.

When a high-speed projectile enters a target of granular materials, it is known that the motion of the projectile depends on the striking velocities, with the mechanisms that cause such motions not well understood. To develop a fundamental understanding of the penetration phenomena in granular targets, we developed diagnostic methods in this research program that characterize 1) the evolving loading and deformation fields in the target during penetration, 2) mechanical behavior of the target material under impact loading conditions, and 3) local pressure variations during the penetration of the advancing projectile.

To conduct the impact experiments, a light gas gun was used to launch projectiles into sand targets. To track the projectile motion in the targets, a flash-X-ray system was integrated with the target chamber of the gas gun. To measure the cavity size opened up by the projectile in the target, a particle-tracking method was developed, which also revealed the particle motion near the projectile. To measure the local pressure variations at strategic locations inside the target, we designed and built thin pressure sensors. To minimize the size of the sensing units inside the targets, we developed a wireless communication system. As a continuation of a previous research effort, the mechanical response of a fine sand was determined as a function of strain rate, initial density, moisture levels and hydrostatic pressure.

This report summarizes the technical achievements realized during the performance period of this research program.

15. SUBJECT TERMS

Granular Target, Projectile, X-ray, Continuum level

16. SECURITY CLASSIFICATION OF: Unclassified			17. LIMITATION OF ABSTRACT	18. NUMBER OF PAGES	19a. NAME OF RESPONSIBLE PERSON Wayne Chen
a. REPORT Unclassified	b. ABSTRACT Unclassified	c. THIS PAGE Unclassified	SAR	42	19b. TELEPHONE NUMBER (include area code) 765 494 1788

Standard Form 298 (Rev. 8-98)
Prescribed by ANSI Std. Z39.18

CONVERSION TABLE

Conversion Factors for U.S. Customary to metric (SI) units of measurement.

MULTIPLY──────────────► BY ──────────────► TO GET
TO GET ◄────────────── BY ◄────────────── DIVIDE

angstrom	$1.000\ 000$ x E -10	meters (m)
atmosphere (normal)	$1.013\ 25$ x E $+2$	kilo pascal (kPa)
bar	$1.000\ 000$ x E $+2$	kilo pascal (kPa)
barn	$1.000\ 000$ x E -28	meter^2 (m^2)
British thermal unit (thermochemical)	$1.054\ 350$ x E $+3$	joule (J)
calorie (thermochemical)	$4.184\ 000$	joule (J)
cal (thermochemical/cm^2)	$4.184\ 000$ x E -2	mega joule/m^2 (MJ/m^2)
curie	$3.700\ 000$ x E $+1$	*giga bacquerel (GBq)
degree (angle)	$1.745\ 329$ x E -2	radian (rad)
degree Fahrenheit	$t_k = (t°f + 459.67)/1.8$	degree kelvin (K)
electron volt	$1.602\ 19$ x E -19	joule (J)
erg	$1.000\ 000$ x E -7	joule (J)
erg/second	$1.000\ 000$ x E -7	watt (W)
foot	$3.048\ 000$ x E -1	meter (m)
foot-pound-force	$1.355\ 818$	joule (J)
gallon (U.S. liquid)	$3.785\ 412$ x E -3	meter^3 (m^3)
inch	$2.540\ 000$ x E -2	meter (m)
jerk	$1.000\ 000$ x E $+9$	joule (J)
joule/kilogram (J/kg) radiation dose absorbed	$1.000\ 000$	Gray (Gy)
kilotons	4.183	terajoules
kip (1000 lbf)	$4.448\ 222$ x E $+3$	newton (N)
kip/inch^2 (ksi)	$6.894\ 757$ x E $+3$	kilo pascal (kPa)
ktap	$1.000\ 000$ x E $+2$	newton-second/m^2 (N-s/m^2)
micron	$1.000\ 000$ x E -6	meter (m)
mil	$2.540\ 000$ x E -5	meter (m)
mile (international)	$1.609\ 344$ x E $+3$	meter (m)
ounce	$2.834\ 952$ x E -2	kilogram (kg)
pound-force (lbs avoirdupois)	$4.448\ 222$	newton (N)
pound-force inch	$1.129\ 848$ x E -1	newton-meter (N-m)
pound-force/inch	$1.751\ 268$ x E $+2$	newton/meter (N/m)
pound-force/foot^2	$4.788\ 026$ x E -2	kilo pascal (kPa)
pound-force/inch^2 (psi)	$6.894\ 757$	kilo pascal (kPa)
pound-mass (lbm avoirdupois)	$4.535\ 924$ x E -1	kilogram (kg)
pound-mass-foot^2 (moment of inertia)	$4.214\ 011$ x E -2	kilogram-meter^2 (kg-m^2)
pound-mass/foot^3	$1.601\ 846$ x E $+1$	kilogram-meter^3 (kg/m^3)
rad (radiation dose absorbed)	$1.000\ 000$ x E -2	**Gray (Gy)
roentgen	$2.579\ 760$ x E -4	coulomb/kilogram (C/kg)
shake	$1.000\ 000$ x E -8	second (s)
slug	$1.459\ 390$ x E $+1$	kilogram (kg)
torr (mm Hg, 0^0 C)	$1.333\ 22$ x E -1	kilo pascal (kPa)

*The bacquerel (Bq) is the SI unit of radioactivity; 1 Bq = 1 event/s.
**The Gray (GY) is the SI unit of absorbed radiation.

Executive Summary

Impact Response of Granular Material at Global & Meso Scales

PI: Weinong Wayne Chen, Purdue University

Co-PI: Dimitrios Peroulis, Purdue University

The objective of this research program is to develop fundamental understanding of the mechanical response of granular target materials under impact loading conditions at two scales: continuum level and particulate level. Complicated interactions between the granular target and a high-speed projectile may produce unexpected projectile motion. A physical and quantitative understanding of the granular material behavior will significantly contribute to the optimal manipulation of the projectile-target interactions in high-speed penetration. In this program, we conducted sand penetration experiments at global scale with the positions of the projectile monitored by flash x-ray. To observe variations in impact-induced pressure inside the sand target, we developed thin pressure sensors that are embedded in strategic locations and wireless communication system to wirelessly connect the sensors to data-acquisition systems.

When a high-speed projectile enters a target of granular materials, it is known that the motion of the projectile depends on the striking velocities, with the mechanisms that cause such motions not well understood. To develop a fundamental understanding of the penetration phenomena in granular targets, we developed diagnostic methods in this research program that characterize 1) the evolving loading and deformation fields in the target during penetration, 2) mechanical behavior of the target material under impact loading conditions, and 3) local pressure variations during the penetration of the advancing projectile.

To conduct the impact experiments, a light gas gun was used to launch projectiles into sand targets. To track the projectile motion in the targets, a flash-X-ray system was integrated with the target chamber of the gas gun. To measure the cavity size opened up by the projectile in the target, a particle-tracking method was developed, which also revealed the particle motion near the projectile. To measure the local pressure variations at strategic locations inside the target, we designed and built thin pressure sensors. To minimize the size of the sensing units inside the targets, we developed a wireless communication system. As a continuation of a previous research effort, the mechanical response of a fine sand was determined as a function of strain rate, initial density, moisture levels and hydrostatic pressure.

This report summarizes the technical achievements realized during the performance period of this research program.
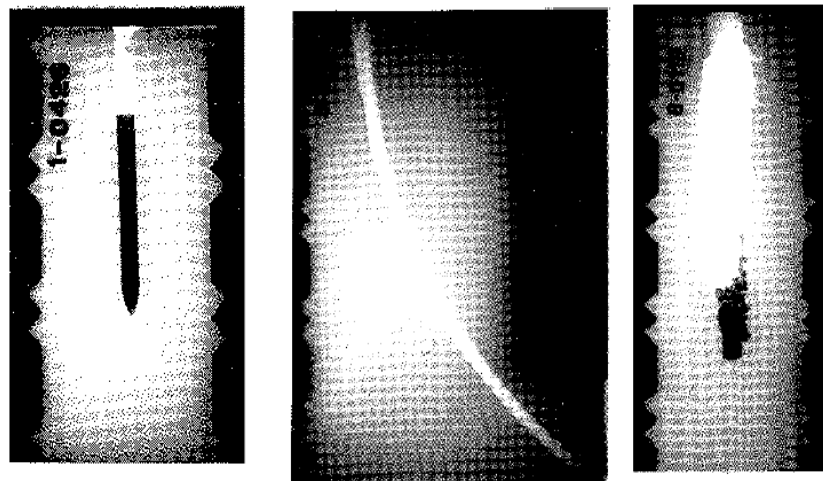
Table of Contents

1. Introduction

1.1 *Background*

When a projectile penetrates through a target, the motion characteristics of the projectile have been observed to change with increasing striking velocity. For example, Piekutowski et al. [1, 2] showed that, at low striking velocities (e.g., below 1 km/s), the penetration of steel projectiles into aluminum targets can be described as a rigid projectile advancing along a straight tunnel of increasing length. As the striking velocity increases to around 2 km/s, the projectile experiences deformation and the tunnel is no longer straight, which deviates the projectile from the intended target. As the striking velocity further increases to around 3 km/s, an eroded projectile is seen in a tunnel of large diameter but short length (Fig. 1). Such striking-velocity

Figure 1: Radiographs of a steel projectile penetrating into an aluminum target (Piekutowski et al., 1999) that shows a rigid projectile motion (left) at a low striking velocity, a curving trajectory in the target (middle) at an intermediate velocity and an eroded projectile (right) at a high velocity.

dependent behavior of the projectile-target interaction poses significant challenges in the development of predictive capabilities for high-speed penetration. Different physical nature is likely responsible for the drastically different penetration behavior.

Similar phenomena are known to occur in other penetration conditions. For example, when a rifle is shooting into a swimming pool, the bullets will shatter (eroded projectile) before reaching the bottom of the pool. However, a lower velocity shot-gun bullet leaves a straight trace traveling through the water. The popular Discovery Channel show "Myth Busters" also showed the difference in the trajectories of a hand-gun bullet and a rifle bullet in ballistic gelatin. In the Impact Science Laboratory at Purdue University, we have observed that the dependence of projectile motion on the striking velocity also occur in other projectile/target combinations. The dividing thresholds for low and high velocities depend on the specific projectile/target combination. For example, when an aluminum alloy penetrator is shot into a wax target, the

turning project in a bent tunnel was observed at striking velocities as low as 150 m/s. We searched the open literature and did not find any documentation that provides the physical nature governing the penetration behavior. Without a thorough understanding of the mechanisms that lead to the changes in penetration patterns, it is not possible to develop physics-based models and reliable predictive capabilities.

When the target is of granular materials, it is expected that similar penetration behavior changes will also occur with increasing striking velocities, although the mechanisms that cause such motions may be very different from those in a metal target. To develop a fundamental understanding, we developed a series of innovative experimental methods the diagnose the dynamic pressure distribution in the target.

2. Technical Approach

2.1 *Development of a Light Gas Gun System*

2.1.1   System Overview

Figure 2: Gas gun system used in the study: Barrel (left) and target chamber (right).

The central piece of equipment in penetration experiments is a light gas gun system. Two images of the gas gun system used in this research are shown in Figure 2. In this design concept, a projectile is launched from the single-stage light gas gun and then enters a target made of a granular material. A flash x-ray system is mounted on the side of the target chamber to monitor the motion of the steel projectile inside the target. Thin pressure sensors are distributed inside the target to record the local pressure histories as the projectile moves by. In an effort to minimize the size of the instrumentation packages, a wireless transmission technology was developed. In the following, the main components of the experimental system are described in more details. Experimental results obtained by the system are illustrated.

2.1.2   Gas Gun

A 63.5-mm diameter light gas was employed to produce consistent projectile launch. The velocity of the projectile is controlled by the pressure in the breech chamber. Figure 3 shows another view of the impact experimental system. When the gas gun discharges the projectile into the granular material target, two pairs of lasers and sensors placed at a fixed distance from each other measure the projectile velocity just before impact. When the projectile hits the target, a flash x-ray system is triggered to record the process of projectile motion inside the target. The projectiles are 12.7 mm in diameter and 50.4 mm in length with semi-spherical noses. The material is 4140 alloy steel. The striking velocities are between 80 and 200 m/s.
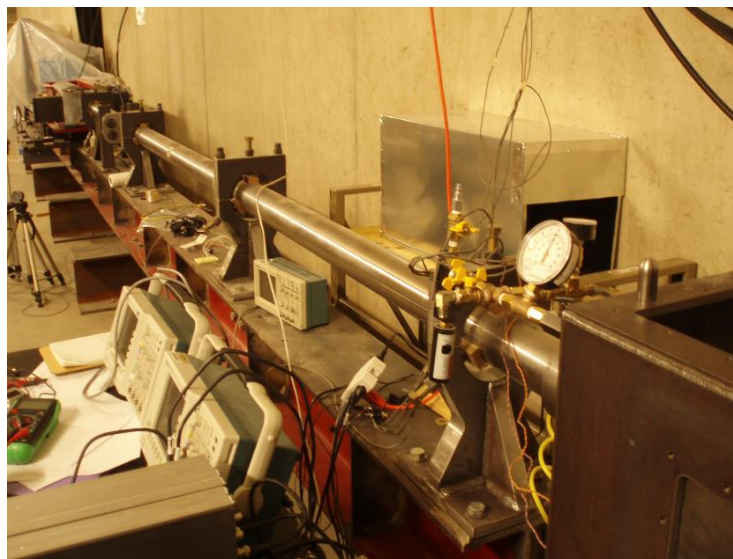
Figure 3: A view of the gas gun system used in the study.

2.1.3   Flash X-ray

To track the projectile motion inside the target, four flash x-ray tubes are mounted on the side of the target chamber. Figure 4 shows the arrangement of the x-ray tubes. To maximize the image resolution, the sand targets are thinner (100 mm) along the x-ray direction. In addition, the sides of the granular targets are made of fiber glass to minimize x-ray attenuation when passing through the granular material container during impact experiments. The x-ray tubes are 150 kV flash x-ray system by L3 Communications. A PixelRay CR2 Desk Top System is placed on the other side of the target to digitally record the x-ray images.
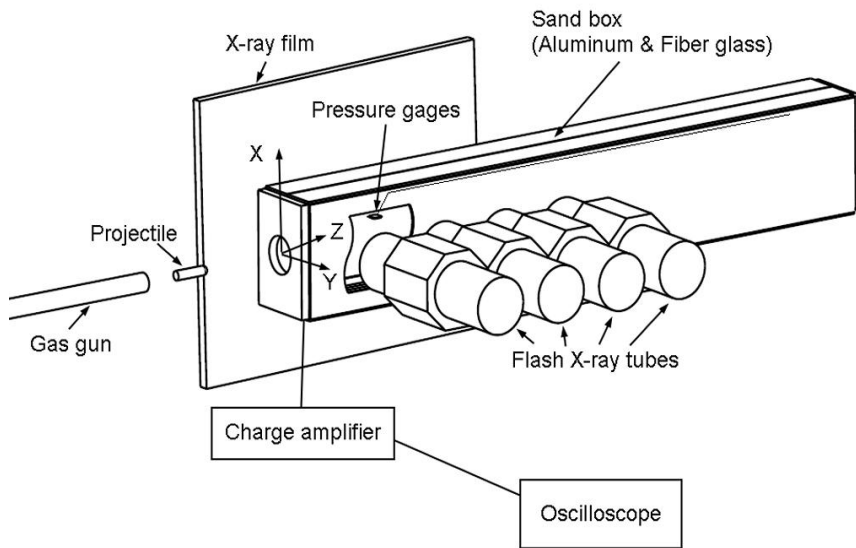
**Figure 4:** The Arrangement of a flash x-ray imaging system.

2.1.4   Projectile Motion inside Target

To record the pressure histories at various locations inside the target, thin pressure sensors are embedded within the target. The arrangement of the pressure sensors has two forms: in a series on one side of the shot line, or symmetrically arranged across the shot line. Figure 5 shows a schematic of the sensor arrangement and an image of the target container after the sensors are installed. The granular material is filled in afterwards.
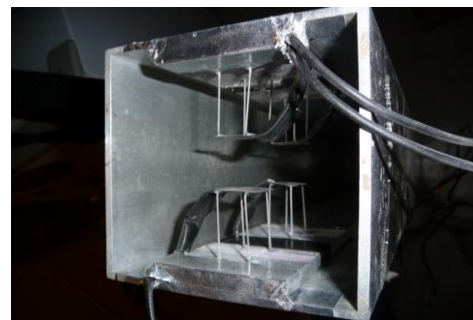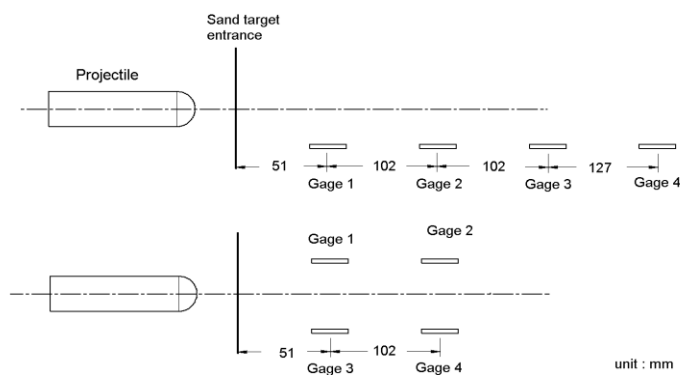

Figure 5: Pressure sensor arrangement inside target.

It was observed in our experiments that, in addition to measuring the pressure histories in the desired positions inside the target, the installation of the sensors might actually affect the motion of the projectiles moving in the velocity range of our experiments. Figure 6 shows a projectile being deflected upwards by the sensors installed below the shot line. Figure 7 shows an opposite case where the sensors are installed above the shot line and the projectile deflects downwards.
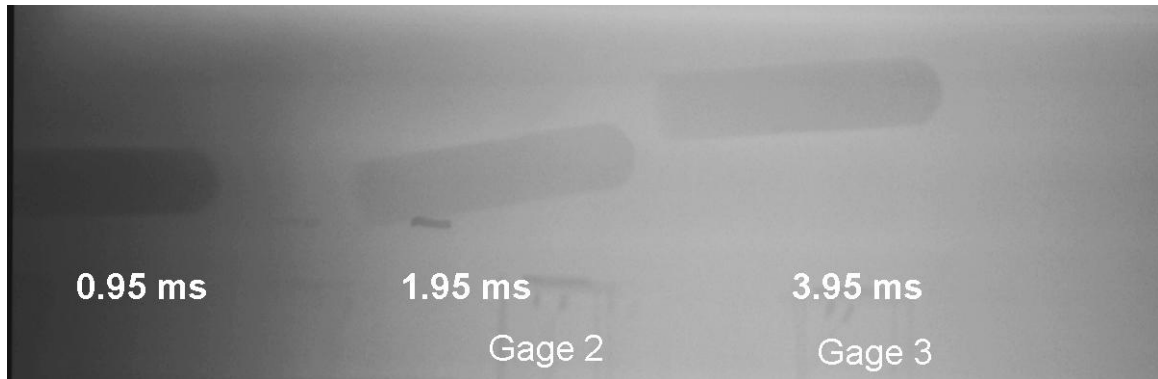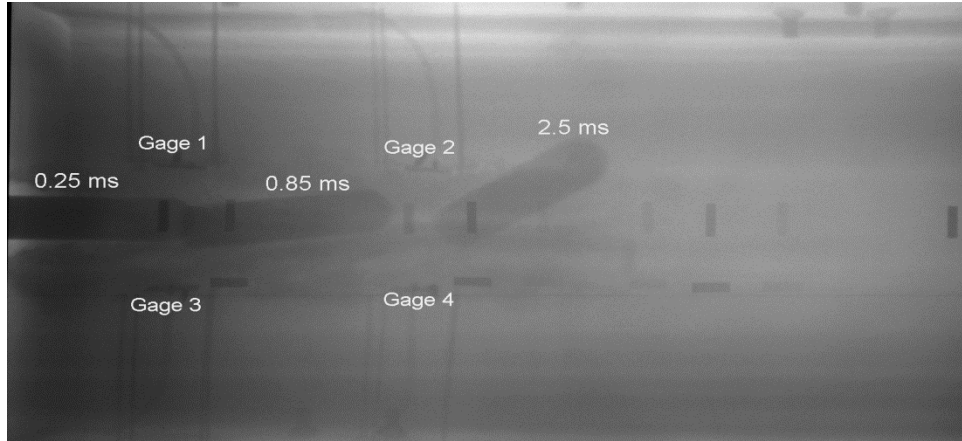

Figure 6: Projectile deflects away by sensors below the shot line.
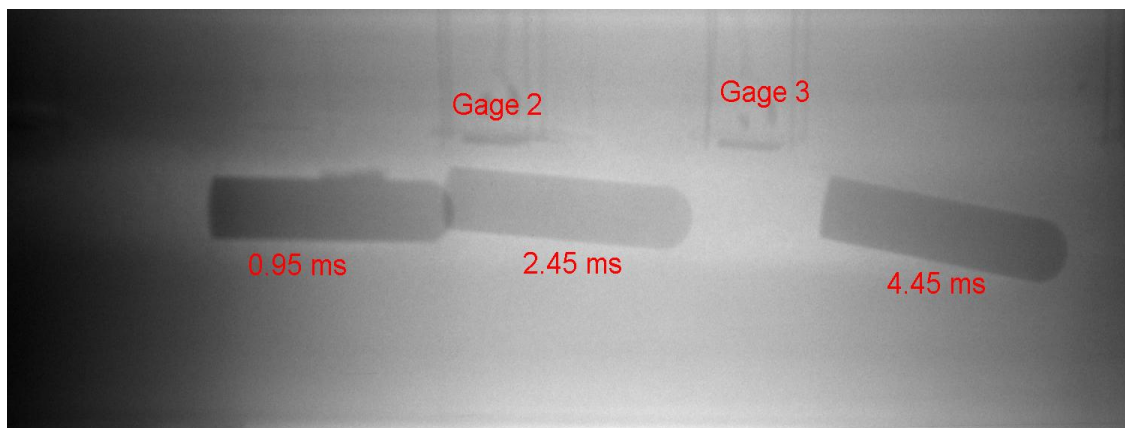
Figure 7: Projectile deflects away by sensors above the shot line.

Figure 8 shows a case of symmetric pressure sensor locations. However, the actual shot line is 3 mm below the centerline of the target. This slight deviation in shot line location causes the projectile to be closer the sensors below the shot line and slightly away from the sensors above, which is considered to be the reason for the projectile to turn away from the sensors below. As will be reported later in the section of pressure sensor, the pressure signal registered on the sensor below the projectile shows a higher value than from the sensor on the top.

Figure 8: Projectile deflects away by sensors below the shot line.

We believe that this is the first time a penetration process is recorded from laboratory experiments where small disturbances in the target configuration cause significant deviation in the desired projector trajectory.

2.2 *Particle Tracking System*

2.2.1 *System Overview*

Radiography with flash x-rays is used routinely in experimental investigation on dynamic behavior of materials [3,4] and is used in our study. Flash X-ray sources produce intense bursts of radiation on objects deforming rapidly. The duration of radiation is less than 100 nanoseconds, which enables clear images of dynamic events occurring at high speeds [5]. Flash X-ray radiography is an effective tool to detect projectile locations in penetration experiments. X-rays pass through low density target materials while being absorbed by high density projectile materials. The resultant shadowgraphs of projectiles record the motion and deformation of projectiles during the penetration inside the targets. The shadowgraphs also show the penetration channels the projectiles created during penetration [1]. In addition to the motion and deformation of the projectile, the motion of the target material around the projectile is also important to be recorded to better understand the penetration event. In targets of granular materials, it is feasible to observe such motion by strategically embedding X-ray opaque particles that can be tracked by radiography. In the experiments conducted by Goldrein et al., lead filling was used as the X-ray opaque material in a sand target to observe the motion of sand during penetration experiments [6]. We designed a special target container that allows iron particles to be embedded in sand targets on to perpendicular planes. The line of intersection of the two planes is the shot line of the projectile. The iron balls have sufficient size to absorb x-ray and achieve satisfactory contrast in radiography. The absorption of X-ray by an object is determined by Beer-Lamber law [7].

$$\frac{I}{I_o} = \exp\left[-(\mu/\rho)\rho t\right]$$

where I_o is the X-ray intensity at the source, I is the intensity behind the material with thickness t, ρ is the density of the material, and μ/ρ is the mass attenuation coefficient. This coefficient is given by reference [7]. In our experiments, we use a 150 keV x-ray system, as described earlier. The mass attenuation coefficients of lead and iron are 2.014 and 0.1964 respectively [7]. If the area density, ρt, of iron is 10.25 times larger than lead, the iron inside sand target generates as high quality of images as those obtained with lead filling. Our trial experiments indicate that 1.6 mm-diameter iron balls embedded in 100 mm-thick sand result in acceptable radiography with the 150 keV x-rays.

In the experiments with the iron particles, we used Ottawa 20/30 sand as a target material and 1.59 mm-diameter iron balls as x-ray opaque particles. These iron balls were distributed in square grids inside sand. Shadowgraphs of the targets with the balls were captured with flash X-rays during penetration experiments. The layers of X-ray opaque material are laid in a horizontal plane when the target is prepared. We designed a special container to place another layers of iron balls orthogonally.

2.2.2 Design of Special Container

Based on our trial experiments on the iron ball size and target thickness for satisfactory x-ray radiography, our container is 11.4 cm by 11.4 cm in cross-section and 91.4 cm-long. For maximum x-ray penetration through the container walls, the walls are made with 12.7 mm-thick polycarbonate and assembled with plastic screws. Figure 9 shows the container and a completed sand target for penetration experiments. The wall consists of eight pieces allowing the container to be separated in two parts from either of the symmetric planes. The container has two inside panels called as a short separator and a long separator. These separators allow the halves of container to hold sand inside without flowing down when the target is separated for particle embedment, as shown in Figures. 10 and 11.
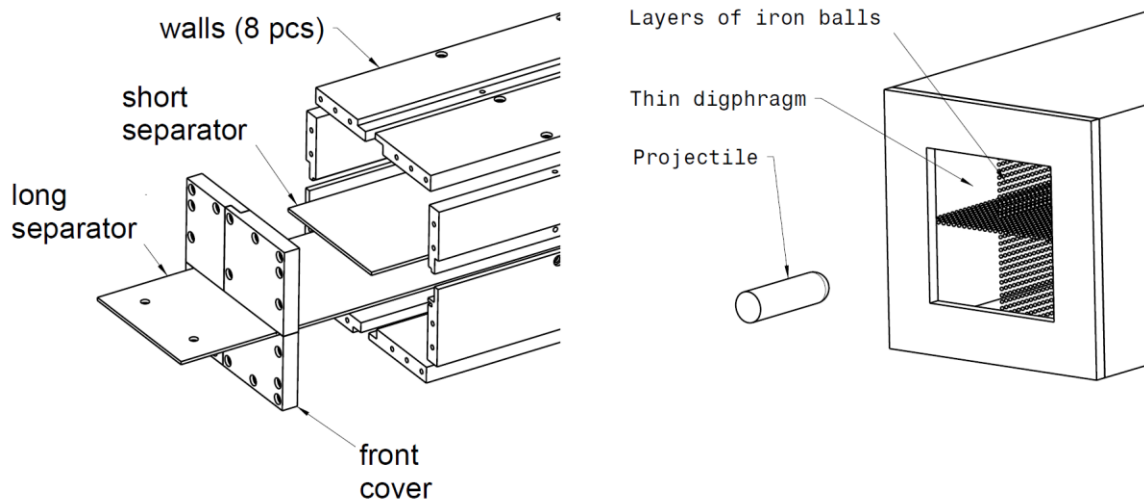
Figure 9: Schematic of a container and fabricated layers of iron balls for penetration experiments.
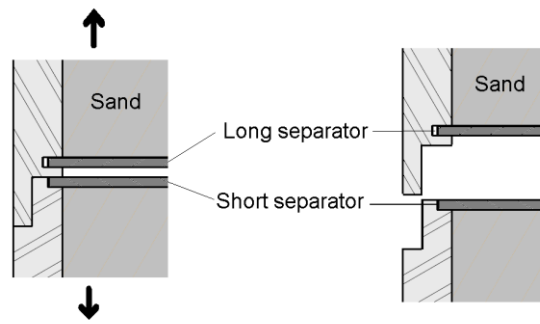
Figure 10: Cross section of two separators to hold sand inside target.
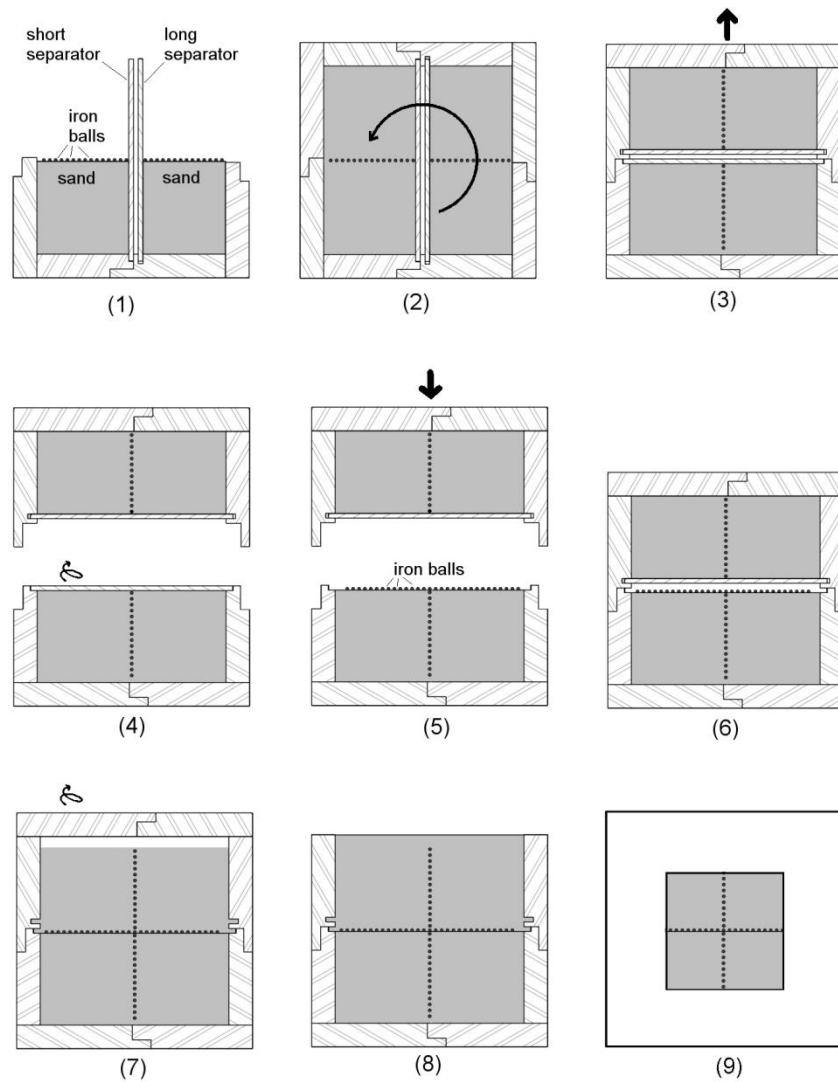
**Figure 11:** Steps to build two orthogonal layers of iron grid.

The short separator is fixed between the upper part and lower part of the container as shown in Fig. 10 and can be removed when these two parts of the target are separated. The long separator is fixed in the grooves in the upper part and can be removed by pulling through the front cover as shown in Fig. 9. Before the target is installed into the target chamber, this front cover is replaced with a new cover having a thin diaphragm to let a projectile enter the target with little resistance during a penetration experiment. This container allows the granular target to have another layer of X-ray opaque particle perpendicular to the exiting layer by rotate the container by 90 °. Figure 11 illustrates the detail procedure to build a sand target with two orthogonal planes of iron balls.

2.2.3   Experimental Procedure

The experimental procedure in preparing a granular material target with two orthogonal layers of metallic particles is explained as follows and illustrated in Fig. 11.

(1) Half of the container is assembled and two separators are inserted vertically. The container is filled with sand on both sides of the separators and iron balls are placed on the open surface of the sand.

(2) The rest of container is assembled and filled with sand. Then, the container is rotated by 90°. The long separator should be on top of the short separator. (Fig. 10)

(3) The container is separated into two parts along the new horizontal symmetric plane.

(4) The short separator is removed by lifting.

(5) Another layer of iron balls is placed on the exposed sand surface.

(6) The upper part of container is placed back on. The entire container is assembled.

(7) The long separator is removed by pulling from the front cover. The sand in the upper part merged with that in the lower part as the separator is removed. The separator should be pulled slowly for minimum disturbances to the iron balls.

(8) The top wall of container is removed. The container is filled completely with sand.

(9) The front cover is replaced with a new cover having a thin diaphragm.
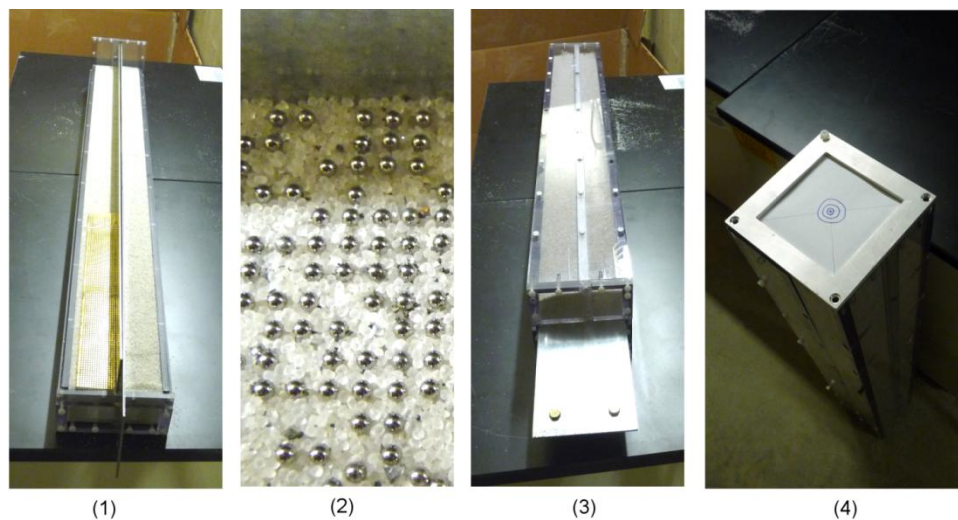

Figure 12: Pictures of the sand container during building.

Figure 12 shows pictures of the container during the building process. Figure 4 (1), (2) and (3) show respectively the lower part of container filled with sand, iron balls on the sand, and long separator being pulled out. Figure 4 (4) shows the replaced front cover with paper for easy projectile entrance.

2.2.4   Experimental Results

To obtain the information on the three dimensional motion of the target medium, x-ray sources are located in both the horizontal and vertical directions from the sides of the container. Figure 13 shows the shadowgraphs of the container in both directions. The images show good quality in terms of contrast and resolutions. In Fig. 13 (1), the left half of iron balls has slight disturbance in from their intended pattern. Sand moved downward when the long separator was pulled out as shown in Fig. 11 (6) and (7). This movement causes the disturbance to the particles already inside the target on the perpendicular plane. However, the disturbance is relatively small and all the iron balls still stay at one plane as shown in Fig. 13 (2).

X-ray in the horizontal
(1)

X-ray in the vertical
(2)
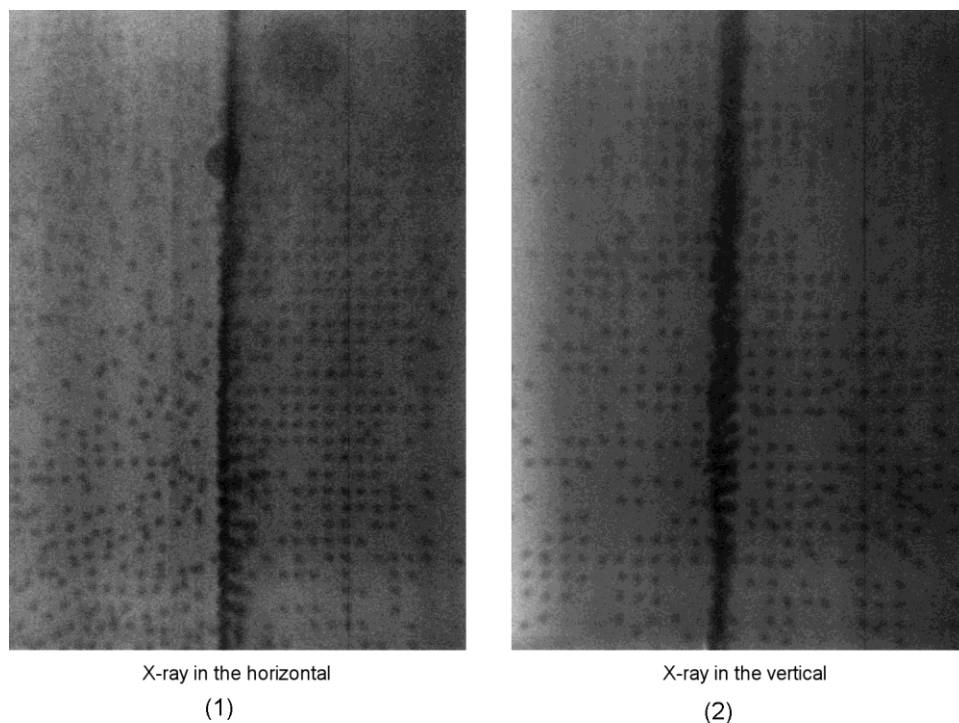
Figure 13: Shadowgraphs of the container in both directions.

Thus, we designed and fabricated a container to build a sand target with two orthogonal planes of iron balls. One layer of iron balls was placed horizontally. After rotating by 90°, another layer of balls was placed. Shadowgraphs of the completed sand target showed satisfactory contrast and resolution of the iron balls in both horizontal and vertical directions. This container is then used in experiments to reveal the tunnel size opened up by the projectile and the motion of particles near the projectile. Figure 14 shows a radiograph where it is clearly seen that the tunnel size

varies with the projectile velocity. When the projectile just enters the target, it opens up a tunnel about three times the diameter of the projectile. However, the tunnel diameter decrease continuously as the projectile slows down.
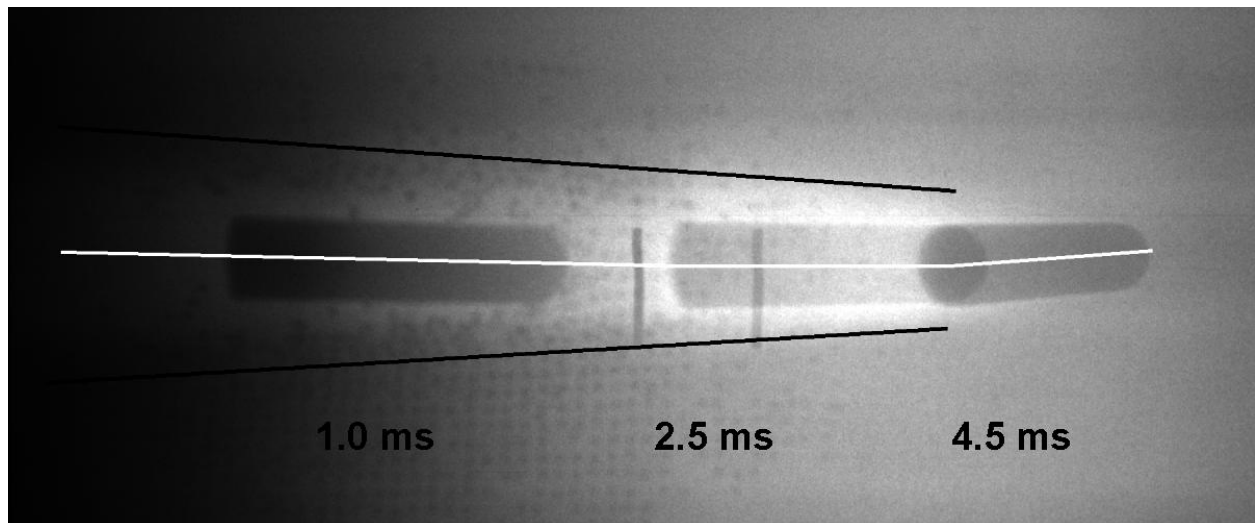
Figure 14: Radiograph showing tunnel size and particle motion.

2.3 *Development of Thin Pressure Gauge*

2.3.1 *System Overview*

As indicated earlier, experimental measurement of dynamic stress propagation in granular materials is required. Stress propagation in granular materials is the primary parameter to be measured in many applications. We developed a pressure gage with Polyvinylidene fluoride (PVDF), a piezoelectric polymer to sense the dynamic stress propagation in sand. The in-house gauge has two brass electrodes to collect generated electric charge and to be connected with a charge amplifier converting the charge into voltage. These PVDF film and brass plates are assembled without any adhesive and wrapped with Teflon tape to minimize response to shear stress. A Kolsky bar was used to calibrate the gauge. The gauge has a constant gage sensitivity under normal stresses up to 50 MPa. The gauge was also embedded in sand sample in Kolsky bar to validate its efficiency in applications. The gauge showed consistent response with respect to the incident pulse. We employed the gauges to measure pressure profiles at strategic locations inside a sand target penetrated by a high speed steel projectile.

2.3.2 Gauge Design

Measurement of dynamic stress in granular materials had many challenges. We designed the pressure gauge meeting the following criteria to obtain accurate measurements.

- Sensing material should have sufficient sensitivity to response to rapidly applied loading.
- The difference of mechanical impedance between a gage and surrounding granular materials should be as small as possible not to disturb wave propagation.
- The gauge should respond to a specific component of stress to analyze the stress vector.
- The gauge should be sufficiently robust not to be damaged by sharp edges of particles.
- The gauge should be sufficiently large to be independent on size of particles.

We employed piezoelectric material which produces electric charge in response to mechanical stress. Polyvinylidene fluoride (PVDF) was selected as the sensing material. The response time of the PVDF is less than 10 ns [8, 9]. PVDF has a low density with 1780 kg/m^3, which is comparable to sand. In this study, we used 28-μm thin-PVDF film which is expected to rarely interfere with the stress propagation.

Figure 15 shows the concept of PVDF gage to measure the stress. The external loading F_e is applied onto the boundary of granular material, and propagates into the gage. The force, F_i applied on the gage cover is generally lower than F_e because the stress is attenuated while propagating. The sources of the attenuation can be friction between particles, inelastic deformation of particles or packing of particles. The rate of attenuation depends on many factors such and void ratio, shapes of particles, density, moisture and so on. Therefore, relation between F_e and F_i is established by empirical methods. The force F_i deforms the piezoelectric material and an electric charge is produced. The generated electric charge is collected through the electrodes attached to the surface of the piezoelectric material. If the material is transversely isotropic and the stress is applied only on the electrodes surfaces, the electric displacements D (C/m^2) are

$$\begin{bmatrix} D_1 \\ D_2 \\ D_3 \end{bmatrix} = \begin{bmatrix} 0 & 0 & 0 & 0 & d_{15} & 0 \\ 0 & 0 & 0 & d_{24} & 0 & 0 \\ d_{31} & d_{32} & d_{33} & 0 & 0 & 0 \end{bmatrix} \begin{bmatrix} \sigma_{11} \\ \sigma_{22} \\ \sigma_{33} \\ \sigma_{23} \\ \sigma_{31} \\ \sigma_{12} \end{bmatrix}$$

$$+ \begin{bmatrix} e_{11}^{\sigma} & 0 & 0 \\ 0 & e_{11}^{\sigma} & 0 \\ 0 & 0 & e_{33}^{\sigma} \end{bmatrix} \begin{bmatrix} E_1 \\ E_2 \\ E_3 \end{bmatrix}$$

where d, σ, e^{σ} and E are piezoelectric strain constant, stress, dielectric coefficient and applied electric field respectively [8]. If the material does not have any electric field, total generated charge is obtained by integrating the electric displacement with the area as

$$Q = \int [D] \, dA = (d_{15}\sigma_{31})A_1 + (d_{24}\sigma_{23})A_2 + (d_{31}\sigma_{11} + d_{32}\sigma_{22} + d_{33}\sigma_{33})A_3.$$

Since the PVDF film is only 25 μm thick, we can assume that the area A_1 and A_2 are zero. Therefore the generation of charge by mechanical stress is

$$Q = \int [D] \, dA = (d_{31}\sigma_{11} + d_{32}\sigma_{22} + d_{33}\sigma_{33})A_3.$$

Generally, the stress propagation in three dimensional media has six components which are coupled each other. The electric charge Q is generated by both of in-plane stress (σ_{11} and σ_{22}) and out-of-plane stress (σ_{33}), which hinder obtaining a specific component of stress for comparison with proposed models. Therefore, the gauge should be designed to respond to a specific component. If the gauge responds to only normal component of stress (σ_{33}) applying from surrounding granular materials, the total electric charge generated from the gage is simplified into

$$Q = d_{33}\sigma_{33}A_{33}$$

where σ_{33} is the normal stress applied on the electrodes. d_{33} is the gauge sensitivity, the ratio of electric charge to the applied force.
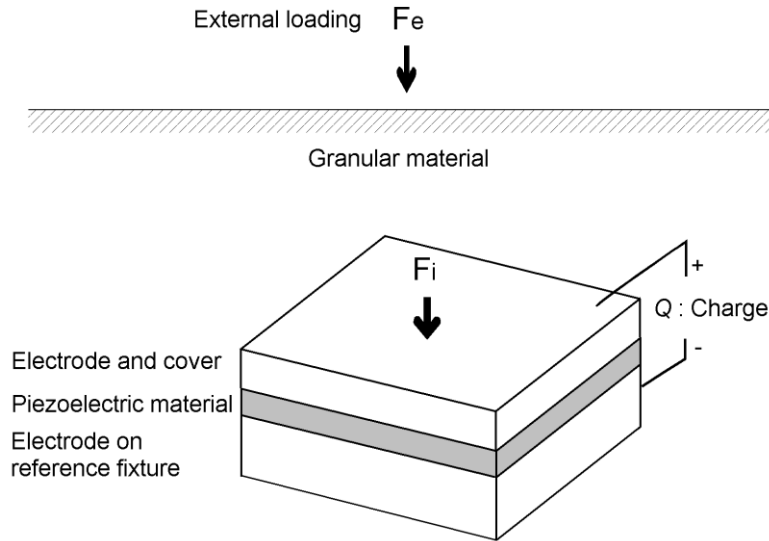

Figure 15: Model of piezoelectric gage response.

As mentioned early in this section, the gage is required to be sufficiently robust in order to resist damage by collision with particles consisting of the granular material. The particle may have sharp edges easily causing damage to the gage. To protect the gauge from the particles, the gauge

should have proper shielding. The shield may affect the gauge sensitivity. Thus, calibration of a gauge package including shielding is required.

Since granular materials consist of small particles, the gage is required to have sufficiently large sensing area to produce consistent results. The gage response is resulted from the sum of interactions between the sensing surface and particles. Rusinek et al. investigated the effect of the ratio of particle size to the sensing area [10]. They showed that the gage response is nearly constant if the gage size is twelve times larger than the size of a particle.

Figure 16 presents the schematic of the pressure gauge we designed for measuring pressures granular materials. The PVDF polymer is 28 μm thick and 8 mm by 8 mm wide. The PVDF film is inserted between two electrodes made with 50 μm-thick brass foils having legs for wire connections. The brass electrode is slightly smaller than PVDF film to prevent electric short by connecting each other. The gauge package is placed on an aluminum plate fixed at a specific position in granular material. The gauge is covered with a 0.38 mm-thick steel plate to protect from sharp edges of particles.
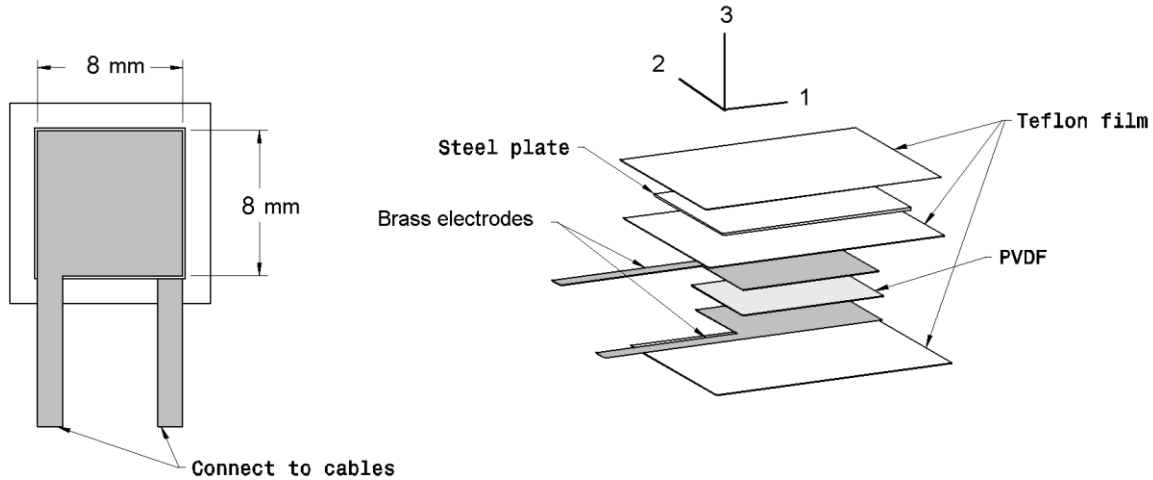
Figure 16: A schematic of the pressure gauge.

The calculation for electric charge is effective only if the gage respond to stress applying in the out-of-plane direction. In-plane deformation of PVDF such as bending breaks down the equation. Therefore, the shield materials should be sufficiently rigid to prevent the erratic gage response. The gauge package should be placed on a rigid plate in applications. PVDF film and brass foils are simply contacted without any adhesive to minimize the transfer of in-plane stress (σ_{11} and σ_{22}) from surrounding media to PVDF film. To hold each layer, the gage is wrapped with 38 μm-thick Teflon tapes. The gauge is connected with a charge amplifier converting generated electric charge into voltage. PVDF only produces electric charge in response to a change in strain. The developed charge decays if the strain does not change. The charge amplifier employs a capacitor and a resistor to reduce the decay. The product of the capacitor and resistor is "time constant" and the voltage signal converted from the electric charge decays by 37% during the time constant. Therefore, the time constants should be carefully decided to observe the change of

voltage with sufficient accuracy. 10 second was selected as time constant based on results from preliminary calibration tests.

2.3.3 Calibration Experiments

Although the piezoelectric strain constants of the PVDF film is published by its manufacturer, the electrodes and shielding affect the gage sensitivity. Moreover, the quantity of generated electric charge of PVDF is known to be nonlinear in response to applied loading. In particular, the piezoelectric strain constants decrease if the material deforms inelastically after yielding. However, if the PVDF deforms elastically, the piezoelectric strain constants remain the same. To calculate the gage sensitivity, specific loading was applied to the gauge, and then the resultant voltage was recorded with an oscilloscope through a charge amplifier. The charge amplifier has a variable sensitivity (pC/N) as a converting factor. The sensitivity was adjusted until the applied external loading agrees with the reported loading from the charge amplifier. The calibration experiments were repeated three times with identical conditions to confirm the consistency in the sensitivities.

To examine the consistency of piezoelectric strain constant of PVDF over a wide range of stress, the gauge response to various levels of hydrostatic pressure was measured. Note that the PVDF yield strength under hydrostatic pressure is much higher than the value under tensile stress (45-55 MPa). The gauge sensitivity can be calculated using $\sigma_h = \sigma_{11} = \sigma_{22} = \sigma_{33}$. The total electric charge and gage sensitivity under hydrostatic pressure are

$$Q_h = \int [D] \, dA = (d_{31} + d_{32} + d_{33})\sigma_h A_3$$

and

$$G_h = \frac{Q_h}{F_h} = d_{31} + d_{32} + d_{33} = -10 \, (pC/N).$$

Figure 17 shows the linear gauge response with respect to the applied hydro static pressure. Intrinsically, PVDF is not adapting material to measure static pressure because the response of PVDF decays with time. Time constant of 100 second is thus used to compensate the decay in the calibration tests with hydrostatic pressure. The obtained gauge sensitivity measured from the results is -10.7 pC/N which is close to -10 pC/N mentioned earlier.

After showing the consistency of the gage sensitivity, calibration tests were conducted with specific amplitudes of dynamic loading to simulate the loadings in applications. The gauge response to uni-axial stress applying onto the faces of the gauge is different from that to hydrostatic pressure. When the gauge is compressed in out-of-plane direction, it expands in in-plane directions due to Poisson's effect. The lateral confinement by packing causes in-plane stress, which affects the gauge sensitivity. Therefore, new gauge sensitivity should be obtained with calibration tests under such loading conditions.
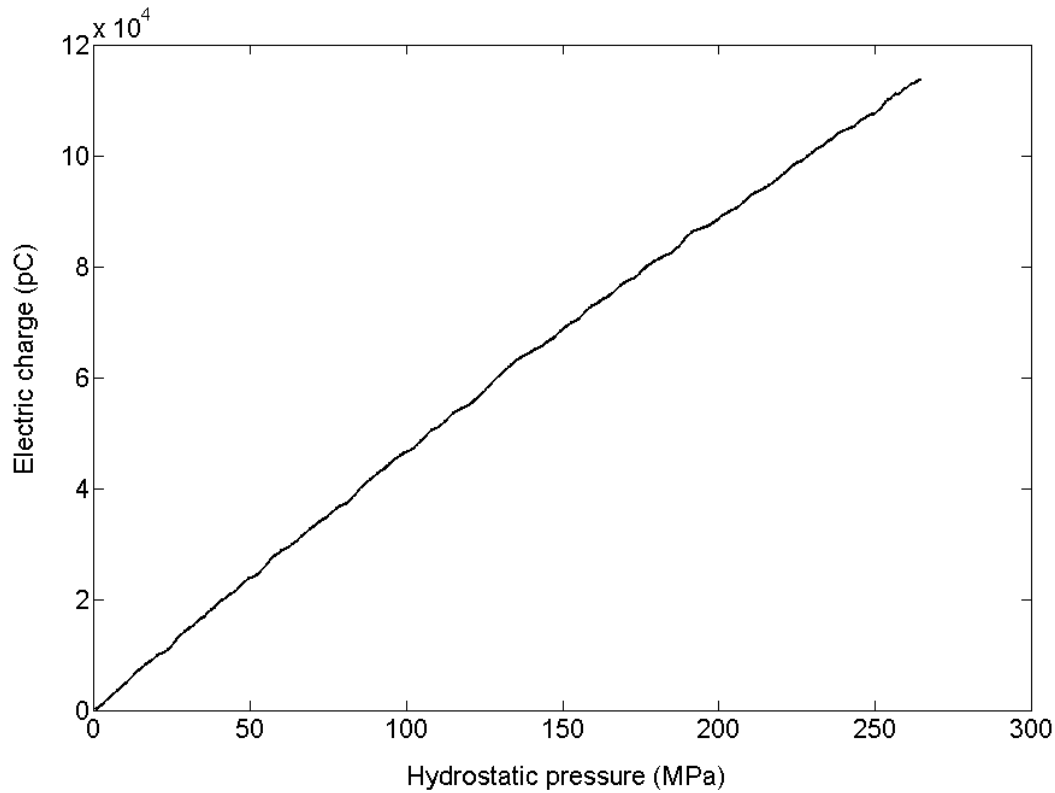
**Figure 17:** Pressure gauge calibration under hydrostatic pressure.
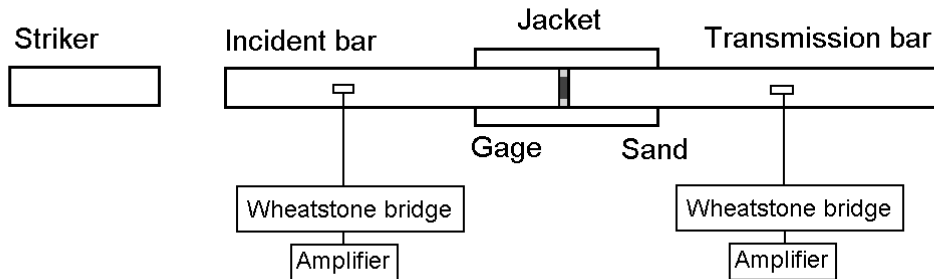
Figure 18: A schematic of Kolsky bar calibration experiments.

A Kolsky bar was employed to apply uni-axial loading on the gage. Figure 18 shows the schematic of a Kolsky bar for the calibration experiments. The striker is projected from a gas gun by releasing compressed gas from a gas tank. The striker hits the incident bar and uni-axial stress propagates along the bar. Then, the stress propagates into the gauge locating between the incident bar and transmission bar. The stress transferred to the gauge can be obtained from the

sum of incident pulse and reflected pulse. Figure 19 shows the incident stress, transmitted stress and the gauge response. The gauge response increases and decreases more than the incident pulse. The obtained gauge sensitivity is -12.5 pC/N. To verify the sensitivity, multiple tests with various levels of loadings were conducted. Figure 20 shows the generated charge from the gauge in response to loading applied by the Kolsky bar. The sensitivity is fairly constant over the various levels of loadings.
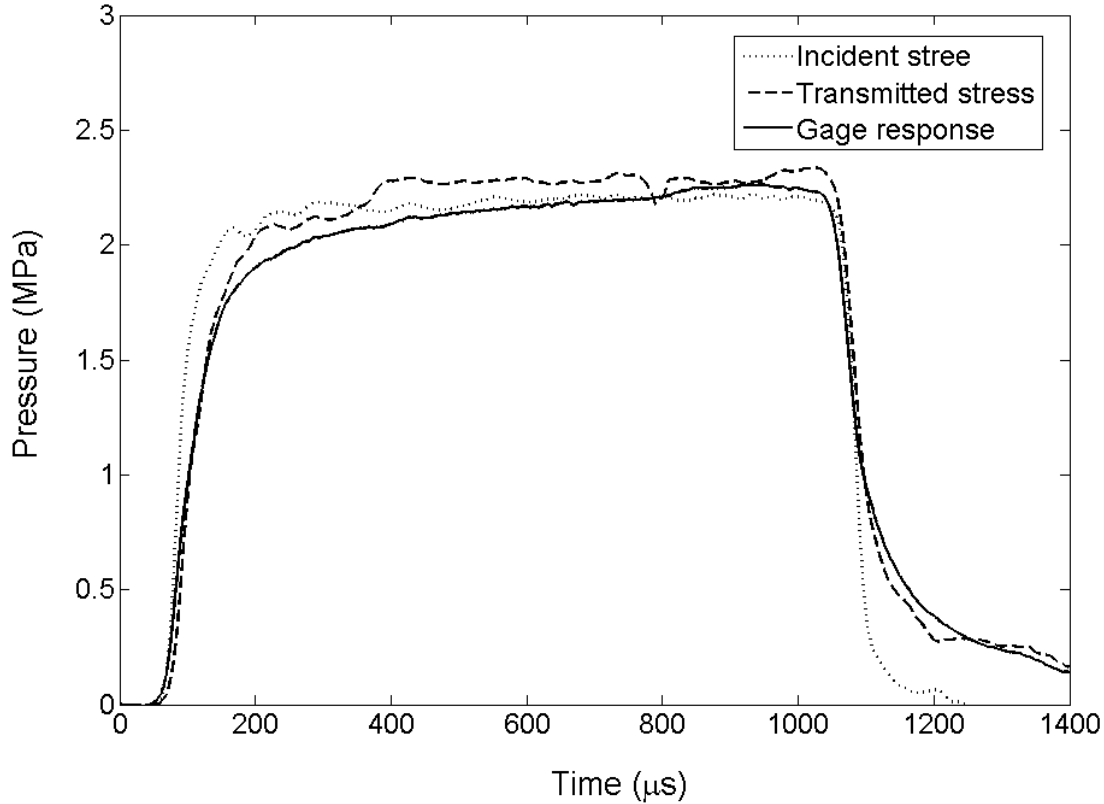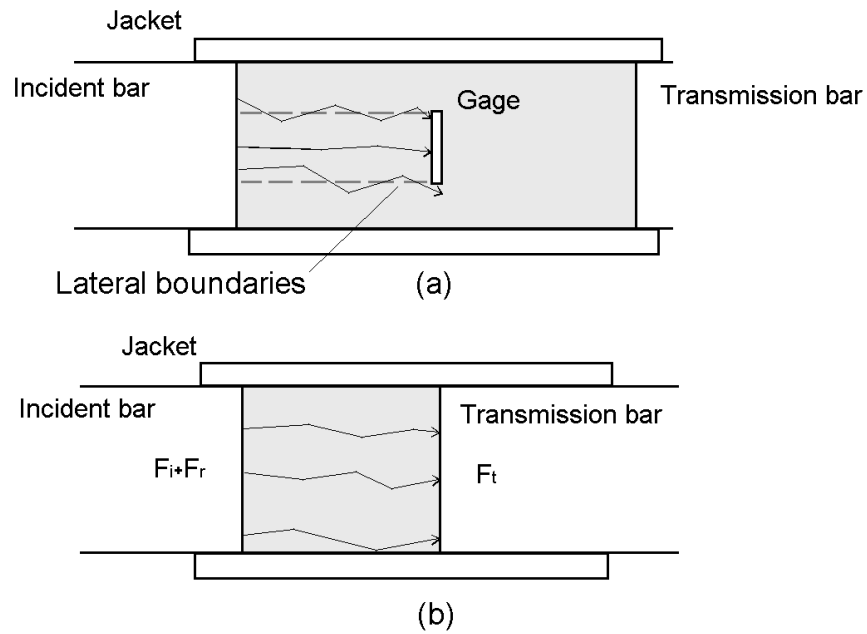

Figure 19: Comparison of gage response, stress from incident bar and transmission bar without sand.

To validate the effectiveness of the gage in granular material, a gage is embedded in sand sample between the incident bar and transmission bar as shown in Fig. 21. The sand sample is confined with an aluminum alloy jacket to achieve quasi uni-axial strain. A specific amount of sand was carefully poured into the aluminum jackets to keep a consistent density. The detailed procedure to prepare the sand is described in the work by Song et al. [11]. We used Ottawa ASTM 20/30 standard sand which consists of 99.8% SiO_2 having a density of 2.65 kg/m^3. The grain has round shape and 98 % of grain sizes ranges from 0.6 mm to 0.85 mm. The bulk density of sand is 1.61 kg/m^3 and corresponding void ratio is 39 %. We varied the length of sand sample by 12.7 mm, 25.4 and 38.1 mm to examine the effect of sand dimension to the rate of stress attenuation.
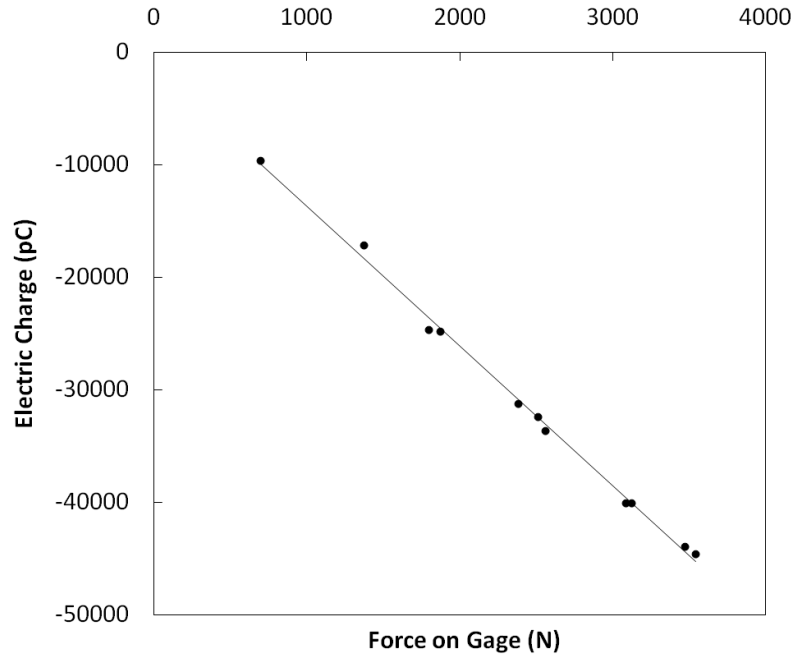
Figure 20: Gauge calibration curve.

Figure 21: Gauge calibration in sand.

(a) 12.7 mm-thick sand

(b) 38.1 mm-thick sand
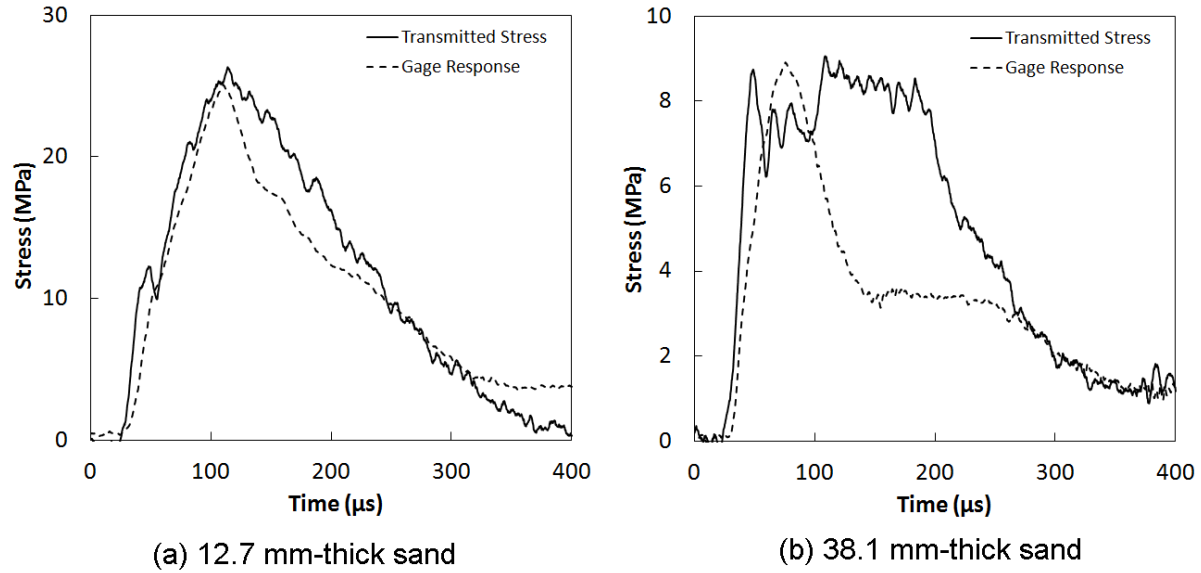
Figure 22: Comparison of gauge output and bar signals.

The gauge response is directly compared with the transmitted stress measured without the gauge. The gauge response in the sand as shown in Fig. 21 (a) is compared with the stress measured in the transmission bar as shown in Fig. 21 (b). Although the length of sand between the gage and the incident bar in Fig. 21 (a) is the same as the length in Fig. 21 (b), the gauge response is not necessarily the same as the stress in the transmission bar. The stress propagation in the sand is not uni-axial because of interaction between particles randomly distributed in sand, which intrinsic characteristics of granular materials.

Since the model of sand under dynamic loading has yet to be established, the calibration experiments should be conducted with simulating the dimension of sand and loading conditions. For instance, one of our applications with the gauge is the measurement of pressure caused by penetration by high speed projectiles. The distance between the projectile and the gauge is comparable to the distance between the incident bar and the gauge in the sand sample in the Kolsky bar. Figure 22 shows the comparisons between the measured stress from the gage and the transmission bar. If the length of sand sample is sufficiently short (12.7 mm), the gage response is close to the stress measured in the transmission bar as shown in Fig. 22 (a) because the disturbance through the lateral boundary can be minimized. However, the measurements do not match each other as shown in Fig. 22 (b) if the length of sand sample is too long.

In this study, we chose the peak stress from gauge response as a parameter to be compared. In most applications such as underground buildings, the maximum stress is the primary parameter affecting the life of structures. Figure 23 presents the peak stress obtained from the gauge and the transmission bar. Note that each peak stress is an average value of three measurements under identical conditions. If the sand sample is as thin as 12.7 mm, the gauge response is lower than the corresponding stress from the transmission bar. The difference between two values decreases as the incident stress increases. If the length of sand sample increases to 25.4 mm, the gauge

response can be higher than the value from transmission bar when the incident stress is around 75 MPa. Both stress are fairly close if the incident stress is around 110 MPa. With higher incident stress around 130 MPa, the gauge response is lower than the value from transmission bar. The trend is similar if the sand length increases to 38.1 mm. The variation in the measured stress ratios reflects the wave attenuation in the sand.
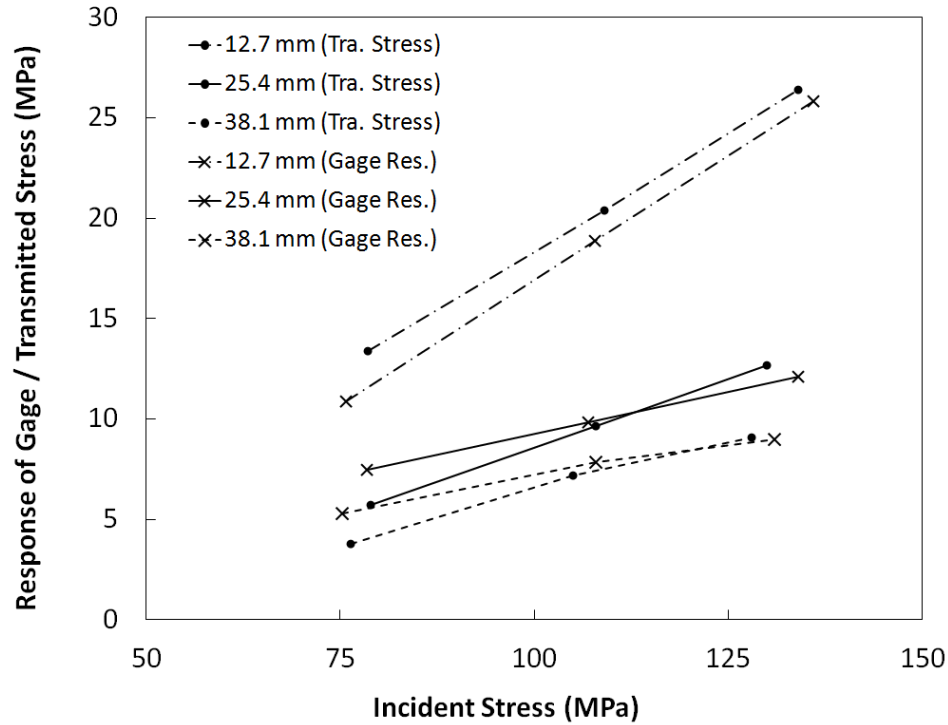

Figure 23: Comparison of peak gauge output and peak transmitted signals.

With the results from calibration tests, we concluded that the response of gauges with respect to the incident pulse is highly affected by the dimension of sand and amplitude of the incident stress. Since empirical equations for the gage response have not been found, calibration tests with considering the dimensions of sand and amplitude of incident stress are required for each application. The stress measured from gage can be lower or higher than the corresponding transmitted value. The deviation become larger if the sand is longer or the incident stress is lower. As the length of sand increases, the force chain in the sand become more complicated and the stress propagation has more complicated path.

To examine the gauge response to stress applied in various directions, the gauge is installed in 0° and 45° with respect to uni-axial stress. Figure 24 shows the gauge directions and corresponding responses installed in three types of degree. The response of gauge installed in 0° shows nearly zero stress over the time. Although the direction of incident stress is perpendicular to the sensing face of gauge, it is supposed to receive shear stress and a small amount of normal stress generated due to the random path of stress propagation. However the components are so small that the gauge has rare response, which is the intention of our design.

The response from gauge rotated by 45° has lower peak stress than the response from gage facing in perpendicular to the incident pulse. However, we cannot guarantee that the peak stress of the tilted gage is a constant proportion of the normal gauge because the deviation of gauge response is as large as the difference between two values. In conclusion, the gauge has reasonably consistent responses with respect to the incident pulse.
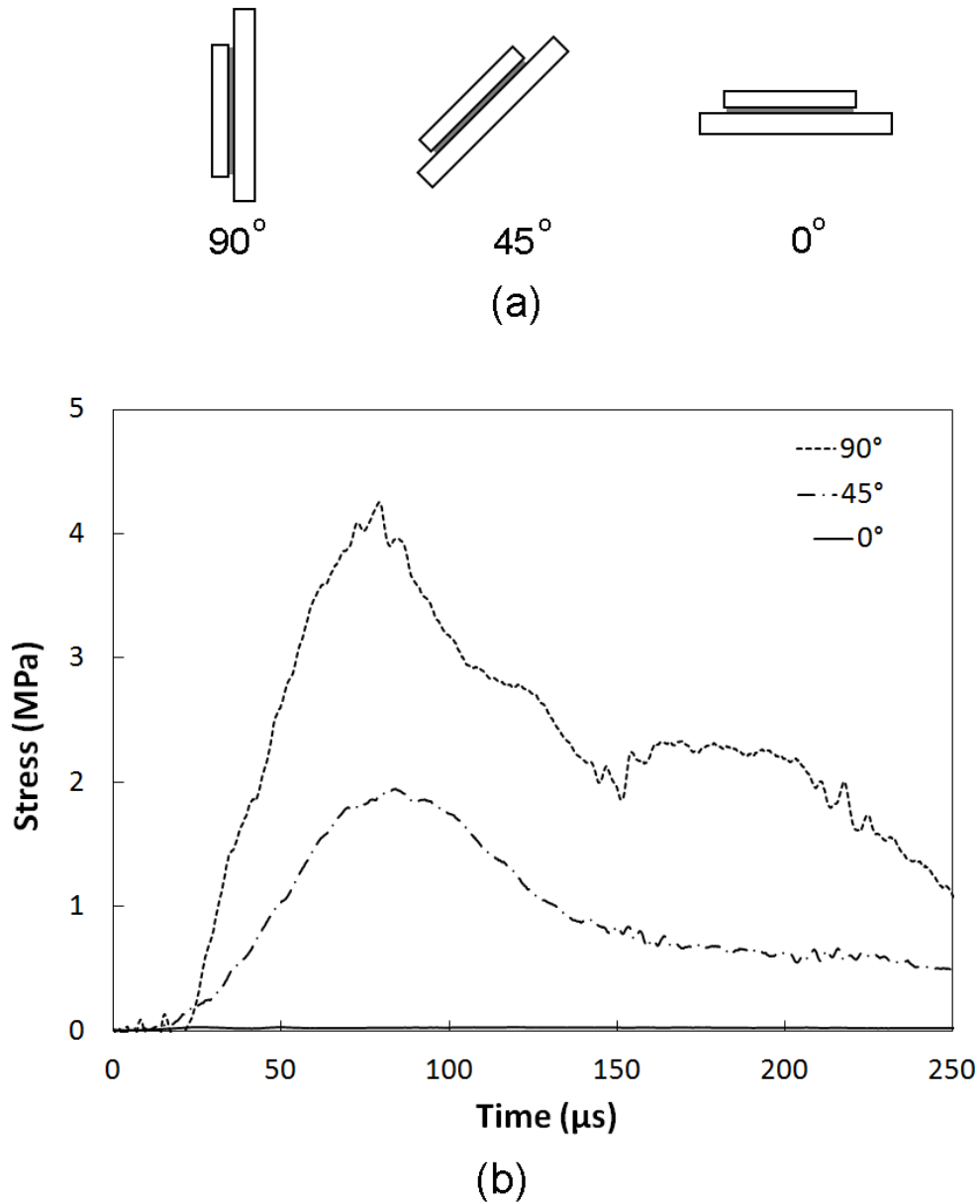

Figure 24: Effects of gauge orientation.

2.3.4   Gauge Application in Experiments

Our in-house gauges were employed in examining propagation of radial stress generated by a projectile penetrating sand target. Gauges were embedded in the sand target with facing center-line in the radial direction as shown in Fig. 25. The cavity expansion caused by the proceed of the projectile generates radial stress, which is to be measured by the gauge [12. 13]. The distance between center-line and gauge is carefully decided to prevent disturbance from cavity generated by the projectile. Gauges are installed in symmetric configuration with respect to the center-line as shown in Fig. 26 (a). Figure 26 (b) presents the stress histories of gauges. Gauge 1, which locates close to the impact surface has the highest stress because the projectile has higher speed than any other locations. Also, the stress profile from the Gauge 1 shows similar shape with the profile measured in calibration experiments. They both have rapidly increasing impulse, plateau and slow decay in time. If the levels of stress and the dimensions of sand in both experiments are close, we can infer that the radial pressure caused by projectile is similar with the incident pulse in Kolsky bar experiments. Gauges 2 and 3 have triangular stress profiles and their amplitudes are much lower than the stress from Gage 1. Since the speed of projectile is lower at the further inside of sand, the radial pressure also decreases. However, the stress from Gauges 2 and 3 are similar even though the speeds of the projectile passing by the two gauges are quite different. More data is needed to investigate the trend of pressure measured in the penetration experiments.
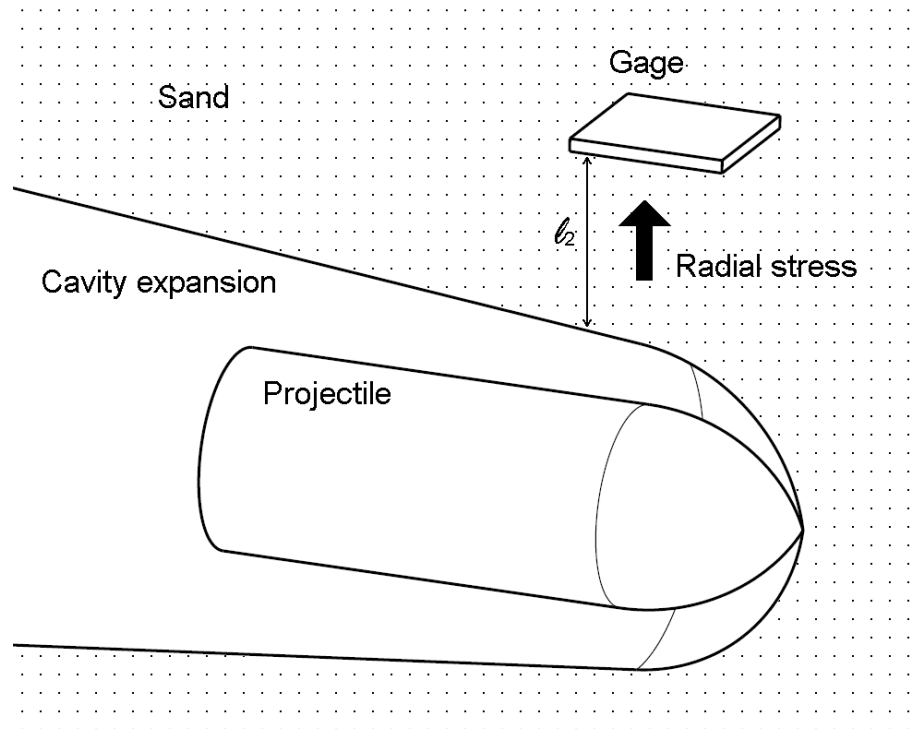
Figure 25: Pressure gauge embedded in target outside of cavity.
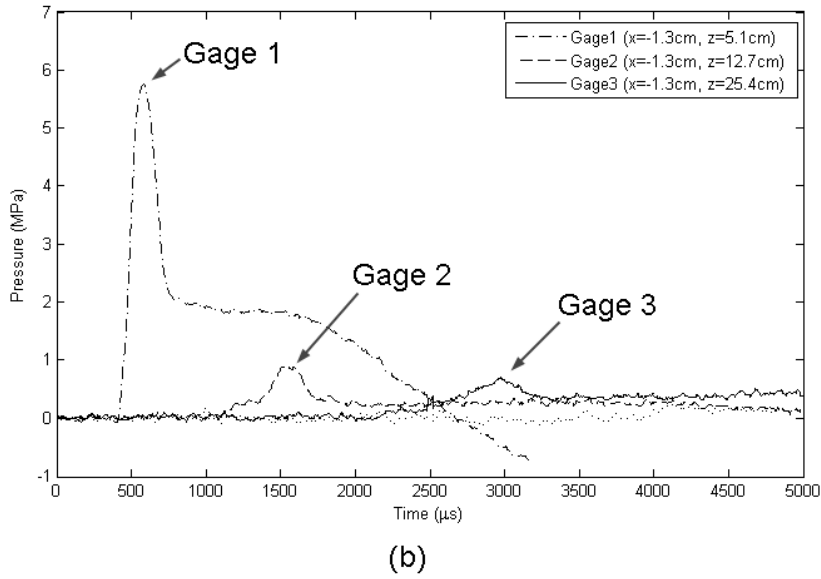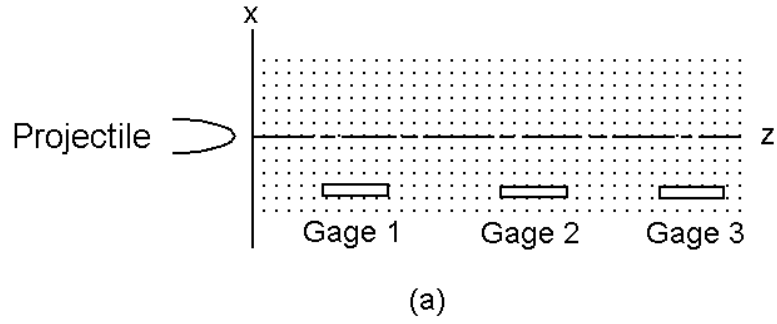
Figure 26: Pressure gauge locations and measured pressure histories.

We thus developed piezoelectric pressure gauges to measure stress profiles in granular materials under dynamic stress propagation. The gauge consists of PVDF film, brass plates and Teflon tape. In Kolsky bar calibration experiments, the gauges show consistent gauge sensitivity and responses with respect to the incident (loading) pulse. The gauges also show reasonably consistent response to the incident pulse when it embedded in sand. We used the gauges in penetration experiments and measured stress profiles in various locations along the depth of penetration in the sand target.

2.4 Wireless Transceiver Circuits

2.4.1 System Overview

The main objective of the circuit presented in this section is to implement a multi-node sensor network capable of high-resolution measurements of an impact response in granular materials. The key requirements to achieve this goal are:
- Size miniaturization: to minimize sensor's effect on granular dynamics
- Wireless transmission: to minimize sensor's effect on granular dynamics
- Multi-node capability: to capture full system dynamics
- High speed, wide dynamic range sensing: to measure large, high speed pressure waves

The limited size of the individual sensor nodes in combination with simultaneous data streams from multiple sensor nodes requires the development of high-density integration and high wireless spectrum efficiency. To achieve these goals, the key developments discussed in this report are:
- Wireless powering with embedded clock: minimizes size by avoiding the use of large battery and crystal oscillator
- Collaborative Orthogonal Frequency Division Multiple Access (OFDMA) wireless transmission: enables many-node network by achieving highly efficient wireless spectrum use
- High-speed analog-to-digital converter: allows high sampling rate

The overall sensor node block diagram is shown in Fig. 27. A base station is used to broadcast a 1.96 GHz wireless powering signal to all of the sensor nodes. The powering signal is rectified and then regulated to provide a stable 1.2-volt supply to power the sensor node's electronics. Additionally, embedded in the powering signal is an 8 MHz clock signal which is demodulated by the sensor node to provide a reference clock to the sensor node.

The sensor to sense pressure data from the impact event consists of a thin piezoelectric polymer pressure sensor. The signal from the sensor is buffered and fed into an analog-to-digital converter (ADC) to digitize the pressure signal. The ADC samples at 2 million samples per second (MSps) and provides 8-bit resolution. The digital signal from the ADC is fed into a quadrature amplitude modulation (QAM) mixer that modulates the phase and amplitude of an RF carrier to encode the digital data and upconvert it to an RF carrier around 3.4 GHz. The signal from the mixer is fed into a power amplifier to transmit the encoded pressure data signal wirelessly to the base station.
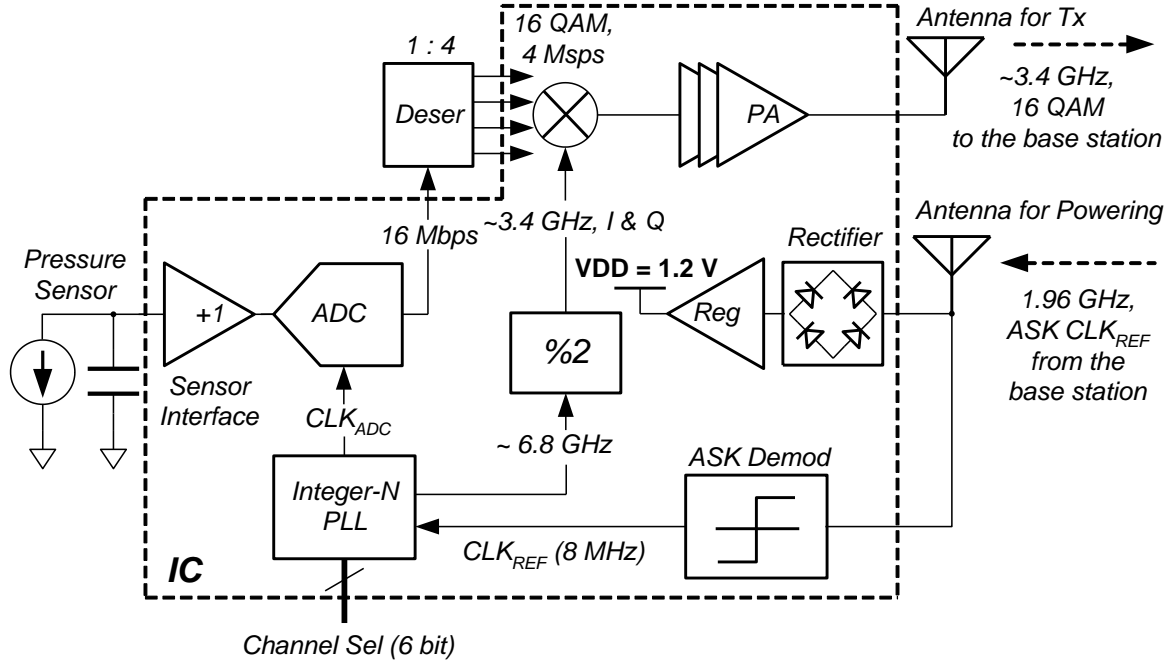
Figure 27: Overall system block diagram.

2.4.2 RF Powering Circuitry

The block diagram of the RF powering and demodulation circuitry is shown in Fig. 28. The powering signal broadcasted from the base station is received at an antenna. The rectifier converts the RF signal received by the antenna into a rectified DC voltage which is limited by a voltage limiter to avoid damage to the sensor node. The rectified voltage is stored on a capacitor. The capacitor supplies a bandgap reference which is used to produce a specific voltage output regardless of the input voltage. The bandgap reference output is connected to the input of a linear regulator used to regulate the voltage at its output to supply the rest of the sensor node with the required 1.2 V for proper operation.

The antenna input is also connected to a separate block which is used to demodulate the 8-MHz clock signal required by the sensor node transceiver. One of the requirements of the overall system architecture using OFDMA is that the clocking signal must have minimum offset between sensor nodes, therefore the clock modulation scheme was chosen to be ASK to enable quick rise time and well-defined clock edges. The demodulator consists of an RC filter which filters out the1.96 GHz signal while keeping the 8-MHz modulation signal. The filtered 8-MHz signal is roughly a square wave as seen in Fig. 26. The filtered 8-MHz signal is fed into a comparator with a fixed threshold. This comparator produces a well-defined square wave at 8 MHz. This demodulated 8-MHz signal is then sent to the sensor node as a reference clock.
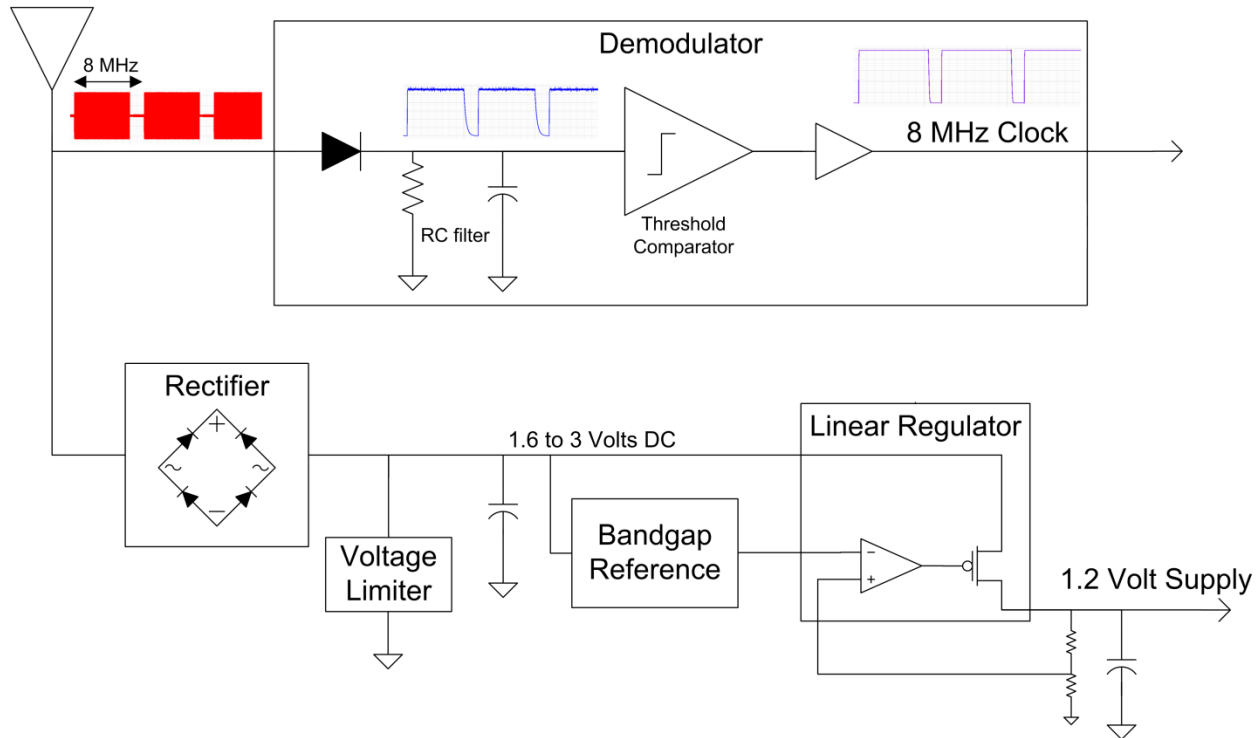
Figure 28: RF powering and demodulation circuitry.

2.4.3 Analog-to-Digital Converter

Figure 27 shows that the pressure sensor is connected to a sensor interface. The sensor interface consists of a unity-gain buffer that provides a buffered version of the voltage on the pressure sensor to an analog-to-digital converter (ADC). To digitize the sensor interface voltage, a successive approximation register (SAR) analog-to-digital converter is used. Its block diagram is shown in Fig. 29. The SAR ADC is chosen for the target application rather than other types of ADCs due to its relatively high speed and high precision, while still achieving low power consumption. The ADC operates as follows. The capacitor array digital-to-analog converter (DAC) is charged to have an equivalent voltage to the input voltage (Vin), the following comparator compares the DAC output with the reference voltage, Vref2, and generates the most significant bit (MSB). After the first comparison, the SAR control logic switches the corresponding capacitor reference voltage, subtracting a binary weighted value from the DAC output, and performs next comparison to generate the following bit. This bit-generation process continues until the least significant bit (LSB) generation finishes, resulting in a digitized bit stream.
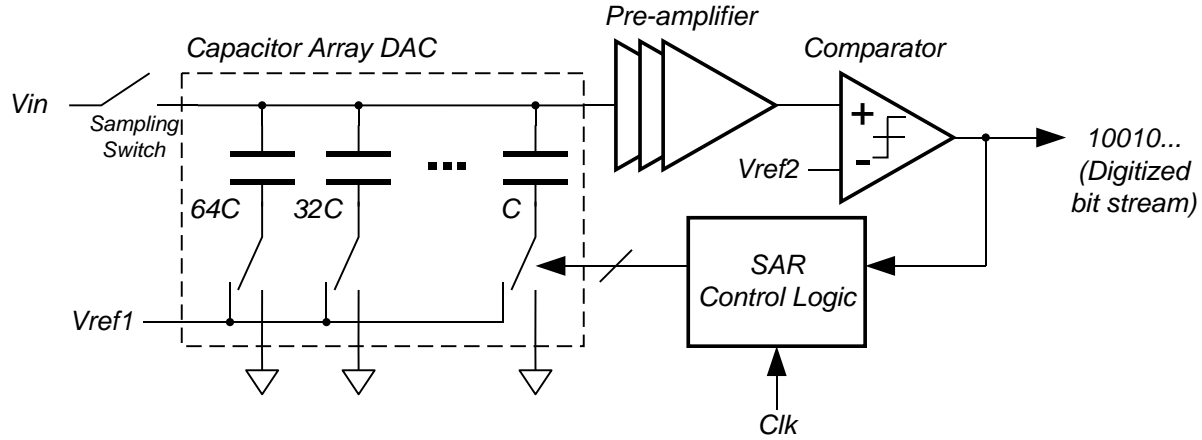
Figure 29: Diagram of successive approximation register (SAR) analog-to-digital converter (ADC).

2.4.4 16-QAM Modulator

Quadrature amplitude modulation (QAM) is a technique used to achieve improved spectral efficiency, at the cost of the reduced bit-error rate (BER). Figure 30 shows the simulated spectrums of a simple binary phase shift keying (BPSK) and 16-QAM signals. The data rates of both modulations are assumed to be 48 Mbps. The simulation shows that the 16-QAM only occupies ¼ the spectrum as compared to the BPSK modulation scheme. To achieve direct 16-QAM topology, a DAC combined mixer structure is used, as shown in Fig. 31. One unit cell mixer is composed of a standard double-balanced gilbert-cell mixer topology, driven by a LO clock as a carrier signal. The input data (D[n]+,D[n]−) is the digitized ADC output, turning on/off the corresponding NMOS switches, implementing a current steering DAC behavior. To achieve a 2-bit DAC structure, two unit cells with binary-weighted current sources are combined in parallel.
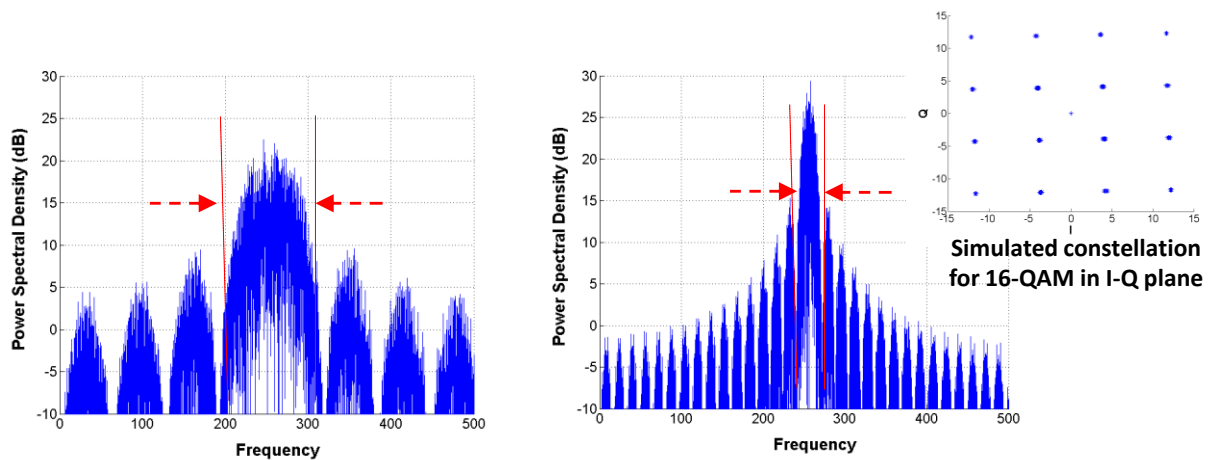
Figure 30: Diagram of (left) BPSK spectrum and (right) QAM spectrum.
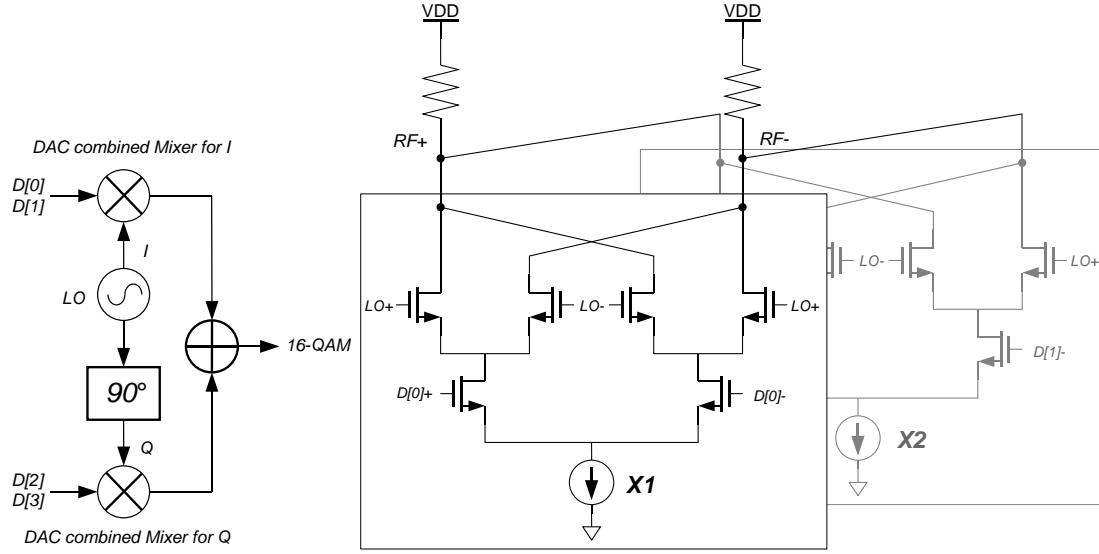
Figure 31: (Left) Diagram of QAM mixer circuit and (right) mixer circuit implementation.
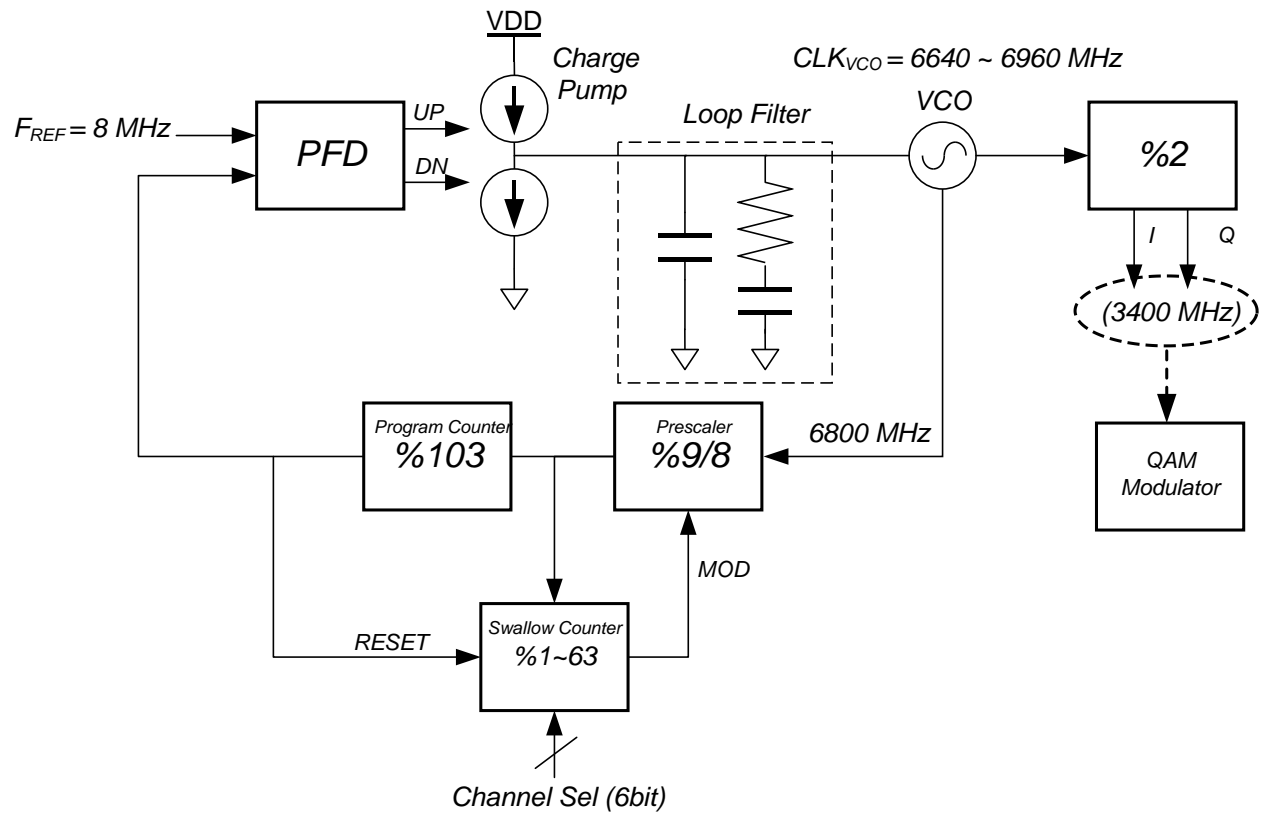
2.4.5 Frequency Synthesizer

An integer-N frequency synthesizer phase-locked loop (PLL) is used to generate a carrier signal. Its structure is shown in Fig. 32. The swallow counter controls the dividing ratio, making the voltage-controlled oscillator (VCO) output frequency programmable: hence the generated clocks can have different frequencies with FREF of frequency separation. For quadrature amplitude modulation (QAM), the voltage controlled oscillator (VCO) operates at twice the RF carrier frequency, and a well-defined in-phase (I) and quadrature-phase (Q) clocks are generated by dividing the VCO output by two. This divide-by-two IQ clock generation approach has an other advantage to prevent injection pulling of the PA output on the VCO, since the VCO operation frequency becomes far from the carrier frequency. One drawback of the standard integer-N PLL is the reference spur interference, which exists at the reference clock frequency (FREF) offset from the operating center frequency. This reference spur is a serious problem, since its location exactly coincides with the center frequency of the adjacent channel, and directly degrades the signal-to-noise ratio (SNR) of the adjacent channel. The magnitude of the reference spur in dBc is:

$$Spur = 20\log_{10} \frac{K_{VCO}v_n}{2F_{REF}}$$

where K_{VCO} is the VCO gain in Hz/V, v_n is the peak magnitude of the VCO frequency control voltage (VCON), measured at FREF. In general cases, FREF is chosen to be equal to the channel frequency separation, which is equivalent to 4 MHz in this application. However, by connecting the divider input to the VCO output directly, FREF can be twice the channel frequency separation (= 8 MHz), allowing 6 dB spur magnitude reduction, as can be verified in the above equation. This approach usually causes significant extra power consumption on the divider due

to the twice increased operation frequency, and often serious in the conventional divider design. In this work, utilizing the newly developed low-power E-TSPC divider, the power consumption penalty is around 1.2 mW, which is not critical compared with the 24 mW power consumption of the entire PLL. In addition, the carrier frequency achieves another 6 dB of spur suppression due to the divide-by-two behavior of the IQ generator. Therefore, overall 12 dB reference spur suppression can be achieved compared with the conventional integer-N PLL frequency synthesizer.

The result of the spur suppression is that sensor nodes in adjacent channels will not interfere with each other as significantly. This is a key development in enabling very high spectrum efficiency, and thus allowing a large number of sensor nodes to operate simultaneously within the limited spectrum.


Figure 32: Diagram of RF frequency synthesizer.

2.4.6 Increased Spectrum Efficiency: OFDMA vs. FDMA

Orthogonal frequency division multiple access (OFDMA) is utilized in this work to further enhance spectral efficiency. The use of OFDMA allows the entire sensor network to occupy half of the bandwidth compared to traditional frequency division multiple access (FMDA). The decreased spectrum is achieved by utilizing orthogonal channel spacing such that adjacent channels do not interfere with each other even while closely spaced. Figure 33 shows the simulated FDMA and OFDMA spectrums for 15 sensor nodes with a 16 MSps data rate. Since FDMA does not allow overlap between different channels, each channel occupies 32 MHz without overlap, thus occupying 480 MHz of overall spectrum. On the other hand, the spectrum of OFDMA allows overlap between adjacent channels. The spectrum usage of OFDMA is 240 MHz, which is half of the FDMA spectrum usage.

 OFDMA is difficult to implement in distributed sensor networks due to the lack of a synchronized clock. However, we have addressed the problem in this work by wirelessly sending the same clock signal wirelessly via the powering signal to each sensor node.
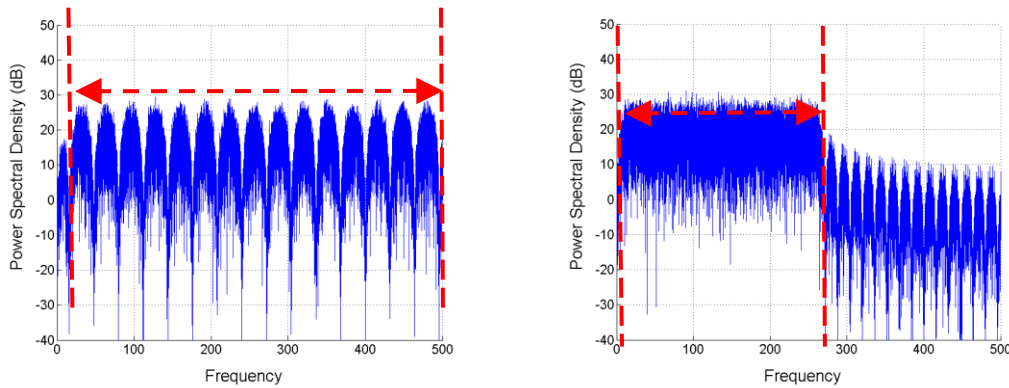
Figure 33: Spectrum of (left) FDMA and (right) OFDMA signals for 15 sensor nodes.

With the successful validation of the contact monitoring, the packaged MEMS device was then connected to the capacitive bounce measurement circuit via the system diagram shown in Figure 38. This is then subjected to the acceleration test using the Hopkinson bar.

2.4.7 Measurement Results

The proposed sensor node was fabricated in 0.13-µm CMOS technology. Fig. 34 shows a microphotograph of the fabricated integrated circuit (IC). On average, the sensor node consumes 43.8-mW of power, delivered wirelessly. A 38-dBm wireless powering signal was transmitted from 13 cm away from the node. To test the functionality of the sensor node, a triangle wave was applied to the sensor input and the spectrum and QAM constellation diagram were measured.

The measurement was performed for a single sensor node, and 2 and 3 sensor nodes operating simultaneously. Figure 35 shows the wirelessly received collaborative OFDMA spectrums and the constellation diagrams of the retrieved 16-QAM data. Figure 33(a) shows the measurement result with a single node operating at the 3.468-GHz channel with a main lobe occupying 8 MHz. The measured error vector magnitude (EVM) from the retrieved constellation is 6.7%. EVM is a measure of how close the constellation point is to its ideal position. An EVM of 0% would mean that the received signal is perfectly centered, however, an EVM of 0% is impractical in real-world environments. When two nodes and three nodes use adjacent channels with 4-MHz spacing, the effective width of the spectrum becomes 12 MHz and 16 MHz, respectively. When three nodes use adjacent channels, the EVM of the retrieved 16-QAM data from the node using the center channel degrades to 9.3% from 6.7% in the single node case. Since the nodes using non-adjacent channels do not cause significant spectrum overlapping, their impact on the EVM would be minimal. Thus adding more sensor nodes will not significantly degrade the network performance.

The measured constellation diagrams show that the 16-QAM operation is successfully implemented. Each point on the diagram represents a 4-bit digital data packet. The 8-bit data from the ADC is represented by taking two consecutive (in the time domain) spectrum points from the constellation.
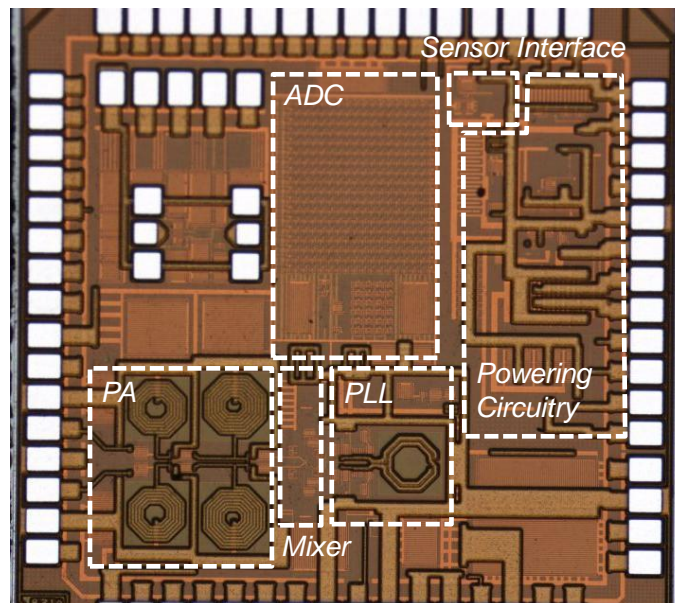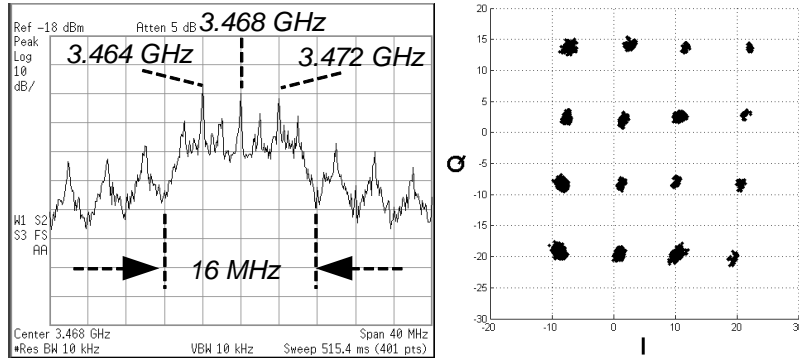

Figure 34: Fabricated sensor node integrated circuit (2mm x 2mm).
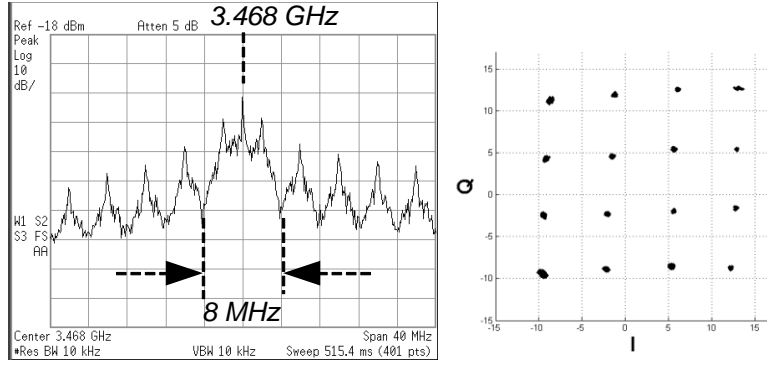
(a) Single sensor node at 3.468 GHz
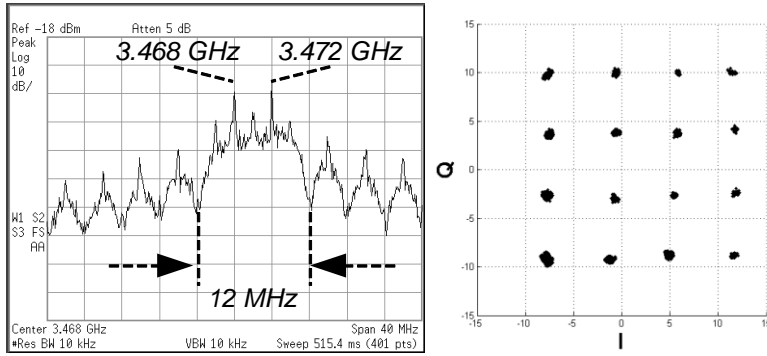
(b) Two sensor nodes operating simultaneously in adjacent channels

(c) Three sensor nodes operating simultaneously in adjacent channels

Figure 35: Measured spectrum and 16-QAM constellations for 1, 2, and 3 sensor nodes.

Thus, a spectrum efficient wireless sensor network and associated sensor node architecture for high-speed measurement of impact response pressures in granular material has been developed. The sensor network implements 16-QAM modulation and an OFDMA multiple access technique to achieve high spectral efficiency, reducing spectrum usage by 8 times compared to the traditional BPSK and FDMA schemes. The increased spectral efficiency is a key development in allowing large data rates from multiple sensor nodes simultaneously. OFDMA is enabled by utilizing a wireless clocking signal for timing synchronization between sensor nodes. Additionally, wireless powering has been implemented in order to minimize system size.

2.5   *Concluding Remarks*

In this study we have successfully demonstrated the concept of instrumented targets in modern penetration experiments. We developed a macroscopic gas gun impact system with flash x-ray system to monitor the motion of the projectile inside a granular target. To reveal the particle motion around the advancing projectile and the cavity size, we developed a system with two perpendicular layers of x-ray opaque particles and demonstrated the effectiveness in penetration experiments. To monitor the local pressure variations when a projectile passes by, we developed thin pressure sensors that are calibrated. The effectiveness of these sensors is demonstrated by recording pressure histories at various locations inside the target undergoing projectile penetration. To minimize the sizes of sensors, we developed a wireless data transmission technology that has been demonstrated to be feasible.

2.6   *Possible Future Directions*

- Systematic penetration experiments should be performed with variables including striking velocity, sensor supporting conditions, sensor location from shot line, and sensor size.
- More detailed calibration experiments need to be performed to quantitatively relate the pressure sensor measurements to the actual pressure environment.
- Wireless data transmission and acquisition systems need to be integrated with the pressure sensors to demonstrate effectiveness.
- Penetration models should be re-visited based on the new information obtained with the improved temporal and special resolutions facilitated by the instrumented target technology.

3. References

[1] A.J. Piekutowksi, M.J. Forrestal, K.L. Poormon and T.L. Warren, "Penetration of 6061-T6511 Aluminum Targets with Ogive-nose Steel Projectiles with Striking Velocities between 0.5 and 3.0 km/s," *International Journal of Impact Engineering*, vol. 23, pp. 723-734, 1999.

[2] M.J. Forrestal and A.J. Piekutowksi, "Penetration Experiments with 6061-T6511 Aluminum Targets and Spherical-nose Steel Projectiles at Striking Velocities between 0.5 and 3.0 km/s," *International Journal of Impact Engineering*, vol. 24, pp. 57-67, 2000.

[3] Zukas JA (1992) Impact Dynamics, Krieger.

[4] Meyers MA (1994) Dynamic Behavior of Materials, Wiley.

[5] Training manual for flash X-ray seminar (2005) L-3 Communications.

[6] Goldrein HT, Grantham SG, Proud WG, Field JE (2001) The study of internal deformation fields in granular materials using 3D digital speckle X-ray flash photography. Proc Shock Comp Con Mat, AIP.

[7] Hubbell JH, Seltzer SM (1996) Tables of X-ray mass attenuation coefficients and mass energy-absorption coefficients from 1 keV to 20 MeV for elements $Z = 1$ to 92 and 48 additional substances of dosimetric interest. NIST Standard Reference Database 126.

[8] R. Kumme and O. Mack and B. Bil and C. Gossweiler and H. R. Haab, "Dynamic Properties and Investigations of Piezoelectric Force Measuring Devices", Kisterl Insturmente AG (2003).

[9] S. O. R. Moheimani and A. J. Fleming, "Piezoelectric transducers for vibration control and damping", Springer (2006), 9-35.

[10] R. Rusinek and M. Molenda and J. Horabik, "Performance of membrane pressure transducers in granular materials of various particle sizes", Powder Technology (2009), 410 – 414.

[11] B. Song and W. Chen and V. Luk, "Impact compressive response of dry sand", Mechanics of Materials (2009), 777 - 785.

[12] Forrestal, M. J. and Luk, V. K., "Dynamic spherical cavity-expansion in a compressible elastic-plastic solid", Transactions of the ASME. Journal of Applied Mechanics (1988), 275 - 9.

[13] J. K. Gran and D. J. Frew, "In-target radial stress measurements from penetration experiments into concrete by ogive-nose steel projectiles", International Journal of Impact Engineering (1997), 715 - 726.

4. Publications from This Project

Hwun Park and Weinong Chen, "Stress variations and particle movements during penetration into granular materials," *Society for Experimental Mechanics*, Proceedings of 2011 Annual Conference, June 2011, pp 85- 92.

Hwun Park and Weinong Chen, 2012, "Two orthogonal layers of metal medium in granular materials for 3D speckle shadowgraph by flash X-ray," *Experimental Mechanics*, accepted.

Kabir, Md. E., Martin, B.E., and Chen, W., 2012, "High-pressure and High Strain-rate Response of Dry Sand Under Triaxial Loading," *Internationa Journal of Impact Engineering*, revised.

Jae Hyuk Jang, David Berdy, Wing-Fai Loke, Dimitrios Peroulis, Weinong Chen and Byunghoo Jung, " A Wireless Sensor Network Utilizing Collaborative OFDMA for Real-Time Pressure Monitoring," Microwave Symposium Digest (MTT), 2012 IEEE MTT-S International, submitted May 2012.

Hwun Park and Weinong Chen, 2012, "Piezoelectric gages to measure three-dimensional dynamic stress propagation in granular materials," *Experimental Mechanics*, to be submitted.

DEPARTMENT OF DEFENSE

DEFENSE TECHNICAL
INFORMATION CENTER
8725 JOHN J. KINGMAN ROAD,
SUITE 0944
FT. BELVOIR, VA 22060-6201
      ATTN: DTIC/OCA

DEPARTMENT OF DEFENSE
CONTRACTORS

EXELIS, INC.
1680 TEXAS STREET, SE
KIRTLAND AFB, NM 87117-5669
      ATTN: DTRIAC